

Subgap Dynamics of Double Quantum Dot Coupled Between Superconducting and Normal Leads

Bartłomiej Baran

Maria Curie-Skłodowska University

Ryszard Taranko

Maria Curie-Skłodowska University

Tadeusz Domański (✉ doman@kft.umcs.lublin.pl)

Maria Curie-Skłodowska University

Research Article

Keywords: Dynamical processes, nanoscopic heterostructure, superconducting qubits, multi-mode oscillations

Posted Date: February 15th, 2021

DOI: <https://doi.org/10.21203/rs.3.rs-223103/v1>

License: © ⓘ This work is licensed under a Creative Commons Attribution 4.0 International License.

[Read Full License](#)

Subgap dynamics of double quantum dot coupled between superconducting and normal leads

B. Baran^{1,*}, R. Taranko¹, and T. Domański^{1,**}

¹Institute of Physics, M. Curie-Skłodowska University, 20-031 Lublin, Poland

*bartlobaran@kft.umcs.lublin.pl

**doman@kft.umcs.lublin.pl

ABSTRACT

Dynamical processes induced by the external time-dependent fields can provide valuable insight into the characteristic energy scales of a given physical system. We investigate them here in a nanoscopic heterostructure, consisting of the double quantum dot coupled in series to the superconducting and the metallic reservoirs, analyzing its response to (i) abrupt bias voltage applied across the junction, (ii) sudden change of the energy levels, and imposed by (iii) their periodic driving. We explore subgap properties of this setup which are strictly related to the in-gap quasiparticles and discuss their signatures manifested in the time-dependent charge currents. The characteristic multi-mode oscillations, their beating patterns and photon-assisted harmonics reveal a rich spectrum of dynamical features that might be important for designing the superconducting qubits.

The double quantum dots on interfaces between various external leads have been proposed for implementation of the spin¹ and spin-orbit quantum bits². Specifically, the superconducting qubits³ have been considered as very promising candidates. Main idea behind such superconducting qubits relies on the in-gap bound states⁴. Their possible implementations could protect the parity of Cooper pairs on proximitized superconducting nanoscopic islands⁵. Additionally appealing perspectives for using the proximitized double quantum dots appeared with realizations of the topological superconductors⁶, hosting the zero-energy modes that are protected by symmetry reasons. Such (Majorana-type) quasiparticles have been proposed for constructing the charge qubit in a transmission line resonator (transmon)⁷ and could be incorporated in the gate tunable superconducting qubits (gatemons)⁸. Readout by means of switching-event measurement using the attached superconducting quantum interference devices has revealed quantum-state oscillations with a high fidelity⁹, which seems to be promising for quantum computing.

Static properties of the in-gap bound states formed in the single and/or multiple quantum dots, nanoscopic length atomic chains or semiconducting nanowires and in magnetic islands proximitized to bulk superconductors have been already described in great detail (see Refs.^{10–12} for survey). As regards their particular realizations in the double quantum dots (DQDs), they have been probed by tunneling spectroscopy using InAs^{13–17}, InSb¹⁸, Ge/Si¹⁹ and carbon nanotubes^{20,21} and by the scanning tunneling microscopy (STM) applied to magnetic di-molecules deposited on superconducting surfaces^{22–25}. These in-gap bound states of DQDs have been investigated theoretically under stationary conditions by a number groups^{11, 18, 26–42}. To our knowledge, however, their dynamical properties have not been inspected yet. We address this issue here because such dynamics could be important for designing future operations on the superconducting qubits.

In what follows, we perform an analysis of the time-dependent observables in the setup, comprising two quantum dots arranged in series between the superconducting and normal metallic electrodes (Fig. 1). We inspect response of this heterostructure to several types of external perturbations, leading effectively either to a melting⁴³ or buildup⁴⁴ of the electron

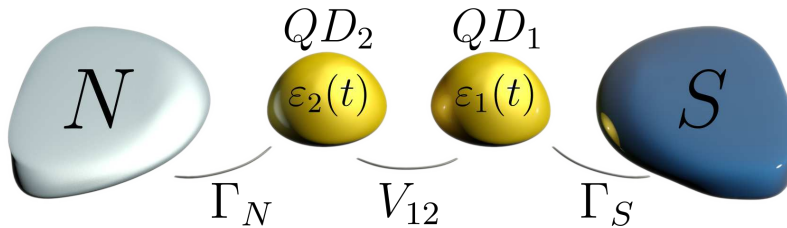


Figure 1. Schematics. Two quantum dots (QD₁ and QD₂) coupled in series between the superconducting (S) and normal (N) metallic reservoirs whose energy levels $\epsilon_{i\sigma}(t)$ could be varied by the external gate potential. We also consider dynamical phenomena driven by the time-dependent bias voltage imposed between the external leads.

pairing. For specific discussion we consider (i) abrupt detuning of the chemical potentials by the source-drain voltage, (ii) quench of the quantum dot energy levels, and (iii) their periodic driving. The latter effect has been recently achieved experimentally in the microwave-assisted tunneling via the single quantum dot in the Josephson-type (S-QD-S) junctions^{45–47}, but similar measurements should be feasible using the N-DQD-S heterostructures as well. Our calculations of the time-dependent electron occupancy and charge currents reveal the damped quantum oscillations whose frequencies coincide with the energies of in-gap bound states. We inspect their nature and determine the characteristic time/energy scales. Furthermore, we show that periodic driving imposed on the quantum dot levels, $\varepsilon_{i\sigma}(t)$, induces the oscillating currents whose conductance (averaged over the period) has a structure reminiscent of the Floquet systems. The dynamical properties studied here could be realized experimentally by applying either *dc* or *ac* external potentials.

Results

We start by discussing the microscopic model of our setup (Fig. 1) and next present the numerical results obtained for three types of the quantum quench protocols. On this basis we infer the typical time-scales, characterizing in-gap bound states that would be valuable for designing some operations on the Andreev qubits. In section *Methods* we also provide some technical details about the computational techniques.

Model and formalism

Our heterostructure, consisting of the quantum dots QD_i ($i = 1, 2$) placed in linear configuration between the normal (N) and superconducting (S) leads, can be described by the following Hamiltonian

$$H = H_S + H_{S-QD_1} + H_{DQD} + H_{N-QD_2} + H_N. \quad (1)$$

We treat the normal lead as free fermion gas $H_N = \sum_{\mathbf{k}\sigma} \xi_{N\mathbf{k}\sigma} c_{N\mathbf{k}\sigma}^\dagger c_{N\mathbf{k}\sigma}$, where $c_{N\mathbf{k}\sigma}^\dagger$ ($c_{N\mathbf{k}\sigma}$) is the creation (annihilation) operator of itinerant electron with the momentum \mathbf{k} and spin σ whose energy $\xi_{N\mathbf{k}\sigma} = \varepsilon_{N\mathbf{k}\sigma} - \mu_N$ is measured with respect to the chemical potential μ_N . The superconducting lead is assumed in the standard BCS form $H_S = \sum_{\mathbf{q}\sigma} \xi_{S\mathbf{q}\sigma} c_{S\mathbf{q}\sigma}^\dagger c_{S\mathbf{q}\sigma} - \sum_{\mathbf{q}} (\Delta_{SC} c_{S\mathbf{q}\uparrow}^\dagger c_{S\mathbf{q}\downarrow}^\dagger + h.c.)$, where Δ_{SC} stands for the isotropic pairing gap. The double quantum dot part is modeled by the single-level localized states

$$H_{DQD} = \sum_{i\sigma} \varepsilon_{i\sigma} c_{i\sigma}^\dagger c_{i\sigma} + \sum_{\sigma} \left(V_{12} c_{1\sigma}^\dagger c_{2\sigma} + h.c. \right), \quad (2)$$

where $c_{i\sigma}^\dagger$ ($c_{i\sigma}$) is the creation (annihilation) operator of electron at i -th quantum dot, $\varepsilon_{i\sigma}$ denote for the energy levels, and V_{12} is the interdot coupling. The quantum dots are hybridized with the external reservoirs via $H_{N-QD_2} = \sum_{\mathbf{k}\sigma} \left(V_{N\mathbf{k}} c_{N\mathbf{k}\sigma}^\dagger c_{2\sigma} + h.c. \right)$ and $H_{S-QD_1} = \sum_{\mathbf{q}\sigma} \left(V_{S\mathbf{q}} c_{S\mathbf{q}\sigma}^\dagger c_{1\sigma} + h.c. \right)$, where $V_{N\mathbf{k}}$ ($V_{S\mathbf{q}}$) denotes the coupling to normal (superconducting) lead.

We restrict our considerations to the wide-band limit (WBL), assuming the constant (energy-independent) auxiliary couplings $\Gamma_{N/S} = 2\pi \sum_{\mathbf{k}/\mathbf{q}} |V_{N\mathbf{k}/S\mathbf{q}}|^2 \delta(\varepsilon - \varepsilon_{N\mathbf{k}/S\mathbf{q}\sigma})$. We also treat the pairing gap Δ_{SC} as the largest energy scale, focusing on dynamical processes solely inside in the subgap regime. Under such conditions the fermionic degrees of freedom of the superconductor can be integrated out, and the resulting low-energy physics can be described by

$$H_S + H_{S-QD_1} \approx \frac{\Gamma_S}{2} c_{1\downarrow} c_{1\uparrow} + h.c., \quad (3)$$

where $\Gamma_S/2$ plays a role of the effective pairing potential induced in QD_1 ¹¹.

In what follows we discuss the time-dependent charge currents $j_{N\sigma}(t)$, $j_{S\sigma}(t)$ and occupancies of the quantum dots imposed by the following types of quantum quenches: (i) abrupt bias potential $V_{sd} = \Delta\mu_N$ applied between N and S electrodes, (ii) sudden change of the energy levels $\varepsilon_{i\sigma}$ due to the gate potential V_g , and (iii) periodic driving of the quantum dot levels with a given amplitude and frequency. Expectation values of the physical observables are computed numerically, solving a closed set of the differential equations (see *Methods*). The charge current $j_{N\sigma}(t)$ flowing between the normal lead and QD_2 can be derived from the time-dependent number of electrons in the normal lead. For $\varepsilon_{N\mathbf{k}\sigma}(t) = \varepsilon_{N\mathbf{k}\sigma}$ this currents is formally given by⁴⁸

$$j_{N\sigma}(t) = 2\text{Im} \left(\sum_{\mathbf{k}} V_{N\mathbf{k}} \exp(-i\varepsilon_{N\mathbf{k}\sigma} t) \langle c_{2\sigma}^\dagger(t) c_{N\mathbf{k}\sigma}(0) \rangle \right) - \Gamma_N n_{2\sigma}(t), \quad (4)$$

where $\langle \dots \rangle$ denotes the quantum statistical averaging and $\langle n_{i\sigma}(t) \rangle \equiv n_{i\sigma}(t)$. The interdot charge flow $j_{12\sigma}(t)$ is expressed as

$$j_{12\sigma}(t) = -\text{Im} \left(V_{12} \langle c_{1\sigma}^\dagger(t) c_{2\sigma}(t) \rangle \right) \quad (5)$$

and finally the current $j_{S\sigma}(t)$ flowing from the superconducting lead to QD₁ can be obtained from the charge conservation law $\frac{dn_{1\sigma}(t)}{dt} = j_{12\sigma}(t) + j_{S\sigma}(t)$. To simplify the notation we have set $e = \hbar = \Gamma_S = 1$ so that energies, currents and time are expressed in units of Γ_S , $e\Gamma_S/\hbar$ and \hbar/Γ_S , respectively. For convenience we assume the superconducting lead to be grounded, treating its chemical potential as the reference level ($\mu_S = 0$). Our calculations are performed for the zero temperature.

Response to a bias voltage

For computational reasons (see *Methods*) it is convenient to assume that initially (for $t < 0$) the quantum dots are disconnected from external reservoirs. Let us briefly discuss the transient current $j_{N\sigma}(t)$ appearing after forming the N-DQD-S heterostructure. In analogy to the previously discussed N-QD-S case⁴⁸ such evolution to the stationary limit is achieved through a sequence of the damped quantum oscillations whose frequencies coincide with the quasiparticle energies of in-gap bound states. In particular, for $\varepsilon_{i\sigma} = 0$ the period of oscillations is equal to $T = 4\pi/\Gamma_S$ whereas the relaxation processes (originating from the coupling Γ_N of QD₂ to the metallic lead) are responsible for damping via the exponential envelope function $e^{-t\Gamma_N/2}$. Practically at times $t \geq 50$ the stationary state seems to be fairly well approached.

We now turn to the dynamical response of N-DQD-S setup caused by biasing at $t = 60$, when the initial chemical potentials are detuned by source-drain voltage $\mu_N - \mu_S = V_{sd}$. Fig. 2b presents the charge currents $j_{N\sigma}(t)$ and $j_{S\sigma}(t)$ obtained for $V_{12} = 2$, assuming $V_{sd} = 1.5, 2$ and 20 (see the legend), respectively. For the large bias voltage, $|V_{sd}| \gg V_{12}$, we observe emergence of the quantum beats with the period $T_B = \pi/V_{12}$ which are superimposed with the higher frequency oscillations. Let us recall, that charge transport is provided here solely by the anomalous particle-to-hole (Andreev) scattering which is sensitive to the in-gap bound states. For the particular set of model parameters the in-gap bound states are formed at energies $\pm \frac{1}{2} \sqrt{4V_{12}^2 + \Gamma_S^2/4} \pm \Gamma_S/4$. It has been previously shown⁴⁹ that the single quantum dot placed between both normal electrodes reacts to a sudden external voltage by the coherent oscillations appearing in the charge current with frequency $\omega = |V_{sd} - \varepsilon_{dot}|$. In the present situation we should replace ε_{dot} by the effective quasiparticle energies at which the Andreev scattering is amplified.

Since we have four such in-gap bound states, the resulting current is a superposition of sinusoidal waves, oscillating with the frequencies $\Omega_{1/2} = V_{sd} \pm \omega_1$ and $\Omega_{3/4} = V_{sd} \pm \omega_2$, where $\omega_{1/2} = V_{12} \pm \Gamma_S/4$. It can be effectively expressed as $\sum_{i=1}^4 a_i e^{-\lambda_i t} \sin(\Omega_i t)$. Individual terms refer here to the damping processes with different parameters λ_i , whereas the coefficients a_i control the contributions from these in-gap bound states. For the large bias $|V_{sd}| \gg V_{12}$ and $\Gamma_S/4$ the quantum beats are superimposed with the faster oscillations. It can be shown⁴⁹ that such beating patterns depend on a ratio

$$r = \frac{\omega_1 + \omega_2}{|\omega_1 - \omega_2|} = \frac{4V_{12}}{\Gamma_S}. \quad (6)$$

For the case displayed in Fig. 2b this ratio is $r = 8$, therefore for $V_{sd} = 20$ the repeated sequences of the beats appearing in the current $j_{N\sigma}(t)$ should be observed with the periods $\frac{\pi}{4}, \frac{\pi}{2}, \frac{\pi}{2}, \frac{\pi}{2}, \frac{\pi}{2}, \frac{\pi}{2}, \frac{\pi}{2}, \frac{\pi}{2}, \frac{\pi}{4}$. For non-integer ratio r the resulting beating pattern is more complicated with the different successive periods.

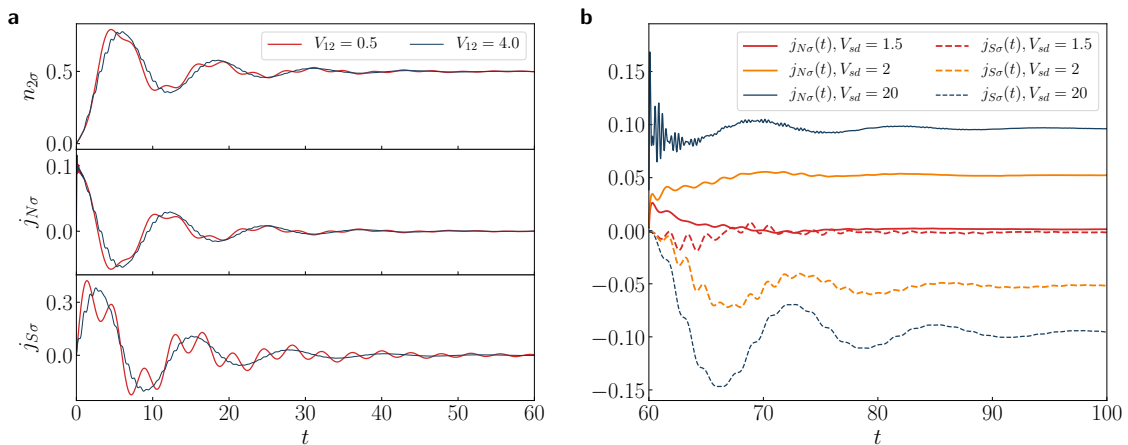


Figure 2. Transient and quench dynamics. a) The time-dependent $n_{2\sigma}$, $j_{S\sigma}$ and $j_{N\sigma}$ obtained for $V_{12} = 0.5, 4$, assuming the initially empty DQDs. b) The charge currents $j_{S\sigma}$ and $j_{N\sigma}$ for $V_{12} = 2$ induced after an abrupt biasing V_{sd} at $t = 60$. Calculations have been done for $\Gamma_N = 0.2$, $\Gamma_S = 1$, $\varepsilon_{i\sigma} = 0$.

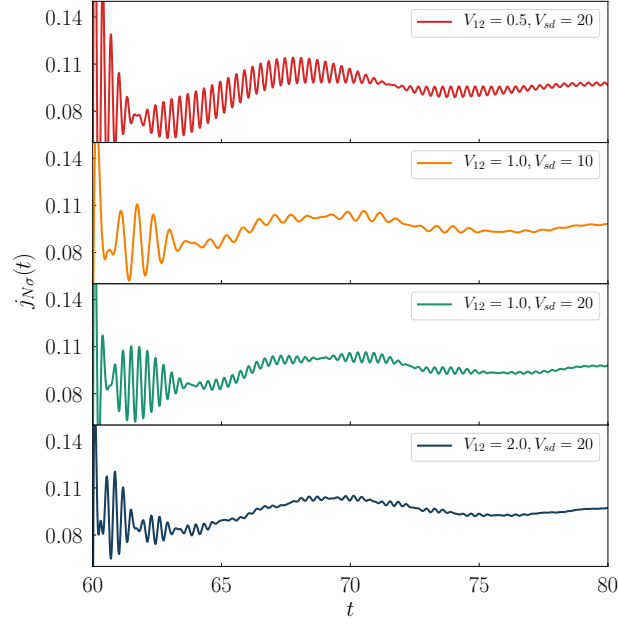


Figure 3. Post-quench beating patterns. The current $j_{N\sigma}(t)$ induced by abrupt biasing at $t = 60$ for several values of the interdot coupling V_{12} and V_{sd} , as indicated. We used the model parameters $\Gamma_N = 0.2$, $\Gamma_S = 1$, $\varepsilon_{i\sigma} = 0$.

Anticipating the behavior presented in Fig. 2b we notice, that for large $V_{sd} = 20$ the post-quench current $j_{N\sigma}(t)$ indeed exhibits the beats mainly with period $T_B = \pi/V_{12}$ superimposed with the faster oscillations whose frequency is equal to V_{sd} . The steady limit current for $V_{sd} = 2$ is larger than for $V_{sd} = 1.5$ because of the broader transport window involving all the in-gap bound states. We also notice that $j_{S\sigma}(t)$ substantially differs from $j_{N\sigma}(t)$, especially for the large bias V_{sd} . We assign this to the fact that DQD sandwiched between the external leads washes out small fluctuations of the current $j_{S\sigma}(t)$, enforcing the final damped oscillations with period $4\pi/\Gamma_S$. Fig.3 displays the beating structure in the time-dependent current $j_{N\sigma}(t)$ after abrupt application of the bias voltage. These beats clearly depend on the interdot coupling V_{12} via $T_B = \pi/V_{12}$. The beating structure is superimposed with oscillations whose frequency is also sensitive to the bias voltage. By measuring the period of such beating oscillations one could thus practically evaluate the inter-dot coupling $V_{12} = \pi/T_B$. For a realistic value $\Gamma_S \sim 200\mu eV$, and assuming $V_{12} = 0.5, 1$ and 2 the beating period would be $T_B \sim 21, 10$ and 5 picoseconds, respectively. This time-scale is currently attainable experimentally.

Quench of energy levels

Let us now consider the dynamics induced by a sequence of quantum quenches imposed on the energy levels $\varepsilon_{i\sigma}$. The first quench $\varepsilon_{i\sigma} \rightarrow \varepsilon_{i\sigma} + V_g$ is performed at $t_1 = 60$, safely after N-DQD-S heterostructure achieves its stationary configuration.

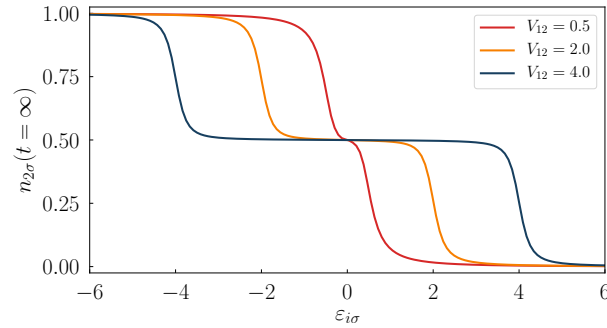


Figure 4. Charge occupancy. The stationary limit ($t = \infty$) occupancy of QD₂ as a function of the energy level $\varepsilon_{2\sigma} = \varepsilon_{1\sigma}$ determined for several interdot couplings V_{12} using the model parameters $V_{sd} = 0$, $\Gamma_N = 0.1$, $\Gamma_S = 1$.

Later on, at time $t_2 = 120$, we rapidly change the energy levels back to their initial values $\varepsilon_{i\sigma} + V_g \rightarrow \varepsilon_{i\sigma}$. Such step-like change (reminiscent of the pump-and-probe techniques) could be practically driven by the external gate potential applied to QDs.

For understanding the dynamics of our setup it would be helpful to inspect the stationary fillings of both quantum dots for several couplings V_{12} . Fig. 4 shows the charge occupancy of QD₂ (the neighbor of the normal lead) with respect to $\varepsilon_{2\sigma}$, assuming that both energy levels are identical $\varepsilon_{1\sigma} = \varepsilon_{2\sigma}$. Since occupancies of both dots are nearly identical, we restrict our considerations to the occupancy $n_{2\sigma}$. We recognize three plateau regions, corresponding to $n_{i\sigma} \approx 1, 0.5$ and 0 , respectively. We also notice, that a width of the half-filling region strongly depends on the inter-dot coupling V_{12} . Variations of the QDs occupancies from the nearly complete filling to half-filling or from the half-filled case to nearly empty QDs occur practically at vicinity of $\varepsilon_{i\sigma} \approx \pm V_{12}$. Change of $n_{i\sigma}$ occur whenever the in-gap bound states coincide with the chemical potential (here $V_{sd} = 0$). Our numerical results obtained for various V_{12} and V_g indicate that the most characteristic time-dependent currents are represented at the middle plateau. Postquench evolution corresponding to the different jump V_g will preserve the same general properties.

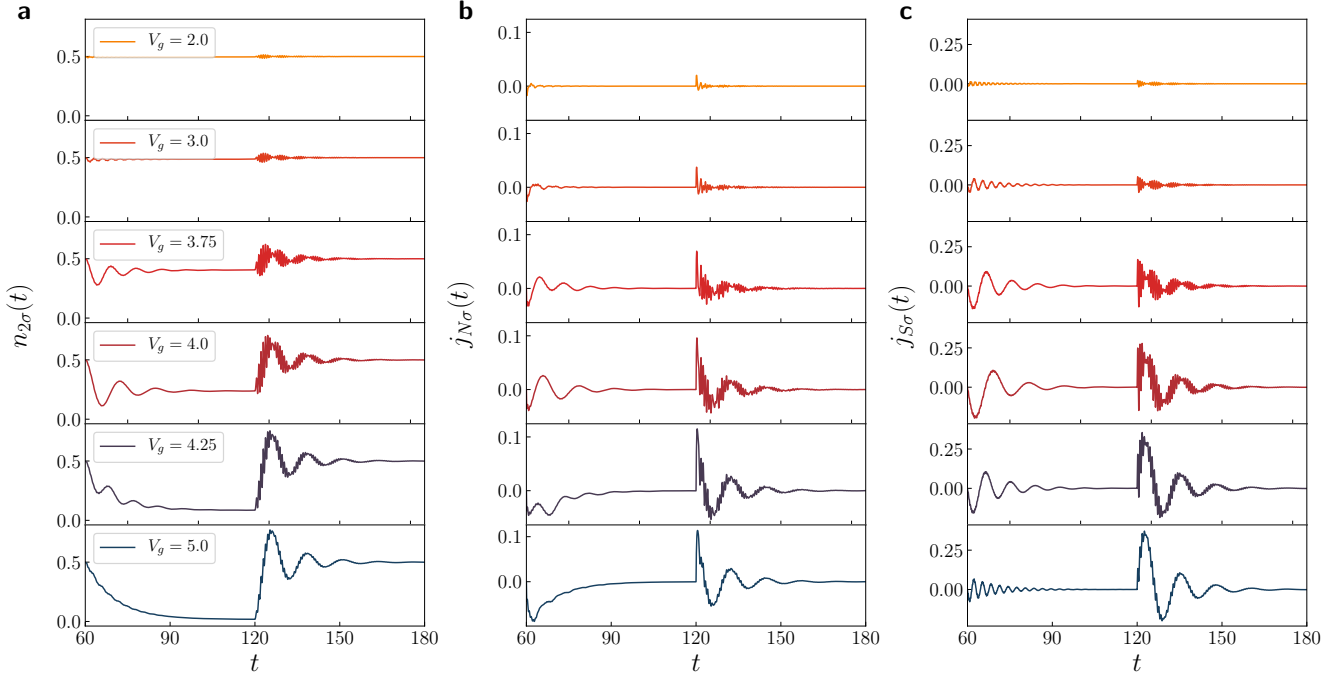


Figure 5. Dynamics imposed by varying the energy levels. The time-dependent occupancy $n_{2\sigma}(t)$ and the currents $j_{N\sigma}(t)$, $j_{S\sigma}(t)$ after step-like variation of the quantum dots energy levels $\varepsilon_{i\sigma} \rightarrow V_g$ at $t = 60$ and $V_g \rightarrow \varepsilon_{i\sigma}$ at $t = 120$. Results are obtained for $V_{sd} = 0$, $\Gamma_N = 0.2$, $\Gamma_S = 1$, $\varepsilon_{i\sigma} = 0$ and $V_{12} = 4$.

In Fig. 5 we show the evolution of $n_{2\sigma}(t)$, $j_{N\sigma}(t)$, $j_{S\sigma}(t)$ obtained for the strong interdot coupling $V_{12} = 4$ after abrupt lifting of the DQD energy levels, at $t = 60$, and their return to initial values, at $t = 120$. More specifically, we have chosen $V_g = 2, 3, 3.75, 4, 4.25$ and 5 , respectively. Let us consider the evolution corresponding to the variation of energy levels from $\varepsilon_{i\sigma} = 0$ to $\varepsilon_{i\sigma} + V_g = 2$, corresponding to the middle plateau (see Fig. 4). The initial QD₂ occupancy is ~ 0.5 and its stationary value after the first quench also equals ~ 0.5 , therefore $n_{2\sigma}(t)$ remains nearly unchanged. Similarly, the currents $j_{N\sigma}$ and $j_{S\sigma}$ are negligibly small (see the upper curves at $t < 120$ in Fig. 5). After the second quench the occupancy $n_{2\sigma}$ is still ~ 0.5 , albeit promptly after the quench we observe some transients exhibiting the beating structure (see the upper curve for $t > 120$ in Fig. 5). This beating structure is more evident for the larger amplitude $V_g = 3.0$ (see Fig. 5 and $t > 120$) for which the occupancy $n_{i\sigma}$ coincides with one of the slopes presented in Fig. 4. We observe the damped oscillations with period $T = \pi/V_{12}$ and the amplitude modulated with another period $T_B = 2\pi/\Gamma_S$. Upon increasing V_g , see Fig. 5 for $t < 120$, the evolution of $n_{2\sigma}$ changes its character from the damped oscillations to the exponential decay, down to nearly zero. Evolution after the second quench (i.e. for $t > 120$) is even more interesting. We observe that the oscillations with the time period $T = \pi/V_{12}$ are well visible for all values of V_g . In addition, the beating structure appears for all values of V_g , except of $V_g = 5$ which refers to the nearly empty QD₂. Notice, that starting from $V_g = 3.75$ (when $\varepsilon_{i\sigma}$ corresponds to a slope of $n_{i\sigma}(t = \infty, \varepsilon_{i\sigma})$), the QD₂ occupancy exhibits additional oscillation with the period equal to $4\pi/\Gamma_S$. The time-dependent $n_{i\sigma}(t)$, $j_{N\sigma}(t)$ and $j_{S\sigma}(t)$ after the second quench ($t > 120$), exhibit similar behavior. We observe the oscillations with period $4\pi/\Gamma_S$ superimposed with faster oscillations whose

period is equal to π/V_{12} , giving rise to the beating pattern with the period $2\pi/\Gamma_S$. Let us inspect more carefully the electron transfer after the first quench, $V_g = 5$ (lowest curves in Fig. 5). The charge current $j_{N\sigma}(t)$ flows all the time to normal lead (till the next quench) in contrast to the currents obtained for smaller quench amplitudes V_g .

Concerning the time-dependent occupancies and currents calculated for $V_{12} \geq 1$, they preserve the qualitative properties discussed above. For the smaller interdot couplings V_{12} (for instance $V_{12} = 0.5$) the evolution after the first quench preserves all properties characterized for stronger V_{12} , but after the second quench we no longer observe the beating patterns, so that only oscillations with the period $4\pi/\Gamma_S$ are present.

Periodically driven energy levels

We now discuss the dynamical response of N-DQD-S heterostructure driven by the periodic driving of the energy levels $\varepsilon_{i\sigma}(t) = A \sin(\omega t)$. This situation can be practically encountered by shining an infrared field on both quantum dots. We assume that amplitude A and frequency ω of the oscillations are identical in both QDs.

In Fig. 6 we present the time-dependent current $j_{S\sigma}(t)$ obtained for $\omega = 0.1$ and two representative values of the amplitude A . The left (a) panel refers to the interdot coupling $V_{12} = 4$, whereas the right (b) panel to $V_{12} = 3$, respectively. For comparison we also present the current obtained for constant value of $\varepsilon_d = 0$ (the top panel of Fig. 6a) which is characterized by the damped quantum oscillations, vanishing in the asymptotic $t \rightarrow \infty$ limit. Similar features, but with different profiles of the quantum oscillations, are also observable for small amplitudes of the periodic driving. They are displayed in Fig. 6a (Fig. 6b) for the interdot coupling $V_{12} = 4$ (3), where the time-dependent current vanishes in the asymptotic limit for the amplitudes $A \leq 3.5$ ($A \leq 2$). Such situation occurs when the amplitude A does not exceed the energies of subgap quasiparticles. This behavior can be contrasted with the large amplitude case (for instance $A = 4$ for $V_{12} = 4$) when the current $j_{S\sigma}(t)$ remains finite throughout all time regions, including the asymptotic limit $t \rightarrow \infty$. We still observe the oscillatory behavior, however its periodicity is more complex.

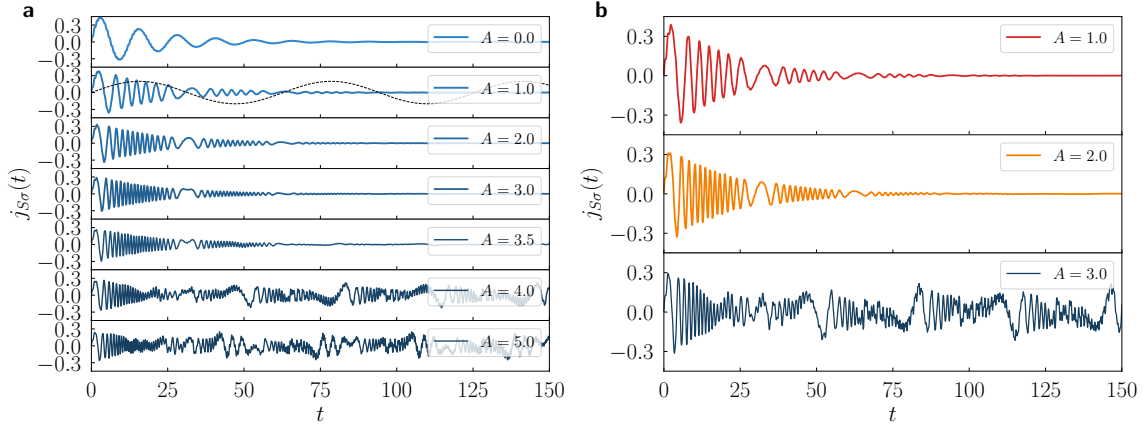


Figure 6. Amplitude effect of periodic driving. The time-dependent current $j_{S\sigma}$ induced by the oscillating energy levels $\varepsilon_{i\sigma}(t) = A \sin(\omega t)$. The panel a (b) presents the results obtained for $V_{12} = 4.0$ ($V_{12} = 3.0$), assuming $\omega = 0.1$, $\Gamma_N = 0.1$, $\Gamma_S = 1$, $V_{sd} = 0$ and several amplitudes A . The dashed line shows the profile of the oscillations energy levels (not in scale).

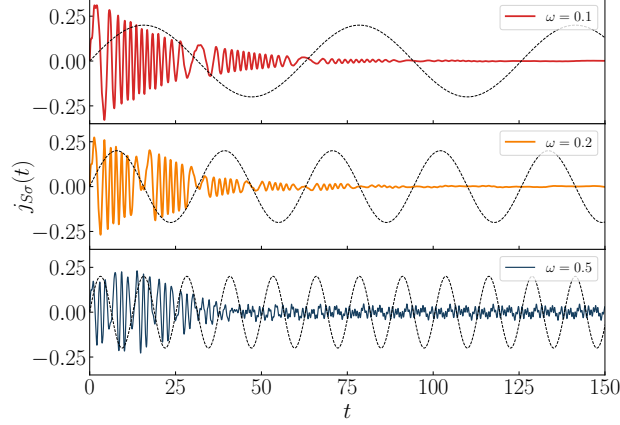


Figure 7. Frequency effect of periodic driving. The time-dependent current $j_{S\sigma}$ caused by periodic driving of the QD levels for several frequencies ω (as indicated), assuming $V_{12} = 3.0$, $A = 2.0$, $\Gamma_N = 0.1$, $\Gamma_S = 1.0$, $V_{sd} = 0$.

In Fig. 7 we present the results obtained for three different frequencies ω , assuming $V_{12} = 3$ and $A = 2$. For this set of model parameters the current $j_{S\sigma}(t)$ asymptotically vanishes for $\omega = 0.1$ and 0.2 (the upper and middle panels in Fig.7), whereas for larger frequencies the oscillations survive over the considerably longer time intervals.

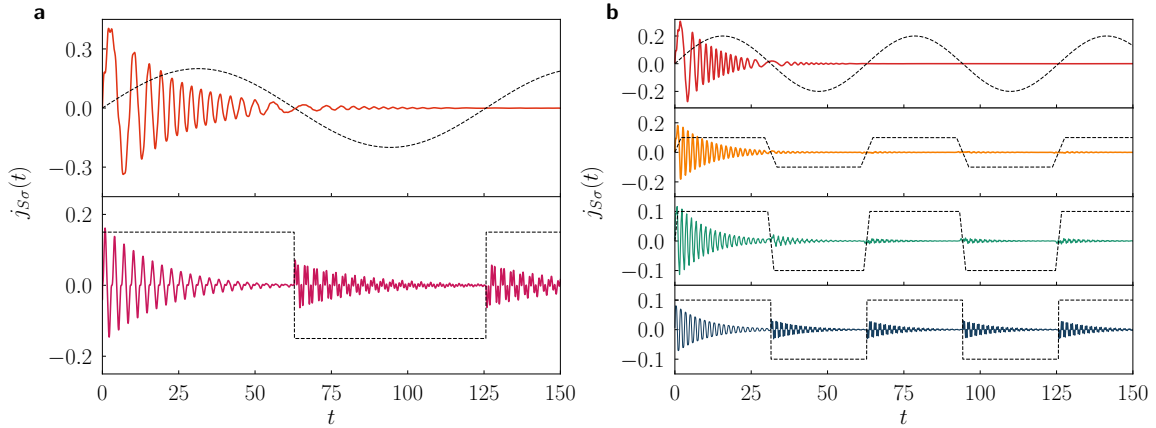


Figure 8. Various protocols of periodic driving. The time-dependent current $j_{S\sigma}$ (solid lines) obtained for different periodic driving schemes $\varepsilon_{i\sigma}(t)$ (dotted lines, not in scale). The panel a (b) shows the results for $V_{12} = 2.0$, $A = 1.0$ and $\omega = 0.05$ ($V_{12} = 4.0$, $A = 2.0$ and $\omega = 0.1$), using the model parameters $\Gamma_N = 0.2$, $\Gamma_S = 1.0$, $V_{sd} = 0$.

Finally we briefly investigate the time-dependent currents imposed by different profiles of the periodically driven energy levels $\varepsilon_{i\sigma}(t) = \varepsilon_{i\sigma}(t + T)$ as depicted by the dashed lines in Fig. 8. For all cases we have assumed the same amplitudes and frequencies. It appears that step-like variations of $\varepsilon_{i\sigma}(t)$ are followed by the damped oscillations. In particular, the right panel in Fig.8 refers to the abrupt lifting/lowering of the quantum dot levels revealing by a sequence of the damped quantum oscillations (after each change).

Andreev conductance averaged over driving period

To get more precise information about the role of amplitude A and frequency ω we inspect here the charge currents averaged over a period $T = 2\pi/\omega$ of the driving field. For specific analysis we focus on the Andreev current $\langle j_{N\sigma}(t) \rangle_{t_0} = \frac{1}{T} \int_{t_0}^{t_0+T} j_{N\sigma}(t) dt$ induced by the source-drain voltage V_{sd} and (in analogy to preceding section) assuming the periodically driven energy levels $\varepsilon_{i\sigma}(t) = A \sin(\omega t)$. From the differential conductance $G_{N,\sigma}(V_{sd}) = \frac{d}{dV_{sd}} \langle j_{N\sigma}(t) \rangle_{t_0}$ one can infer *quasienergies* of the in-gap bound states⁵⁰.

Our main objective is to analyze the quasiparticle features which show up in the measurable nonequilibrium transport properties of N-DQD-S heterostructure. Initially (for $t < 0$) we assume both quantum dots to be empty and next, at $t = 0$, we impose the oscillations of the quantum dot levels $\varepsilon_{i\sigma}(t)$ simultaneously with the bias voltage $\mu_N - \mu_S = V_{sd}$. We choose

t_0 at which the transient effects become negligible. This choice can be arbitrary, because safely after forming N-DQD-S heterostructure the time-dependent current oscillates with the period T as enforced on the energy levels (c.f. Figs. 6-8). Below we briefly discuss the differential conductance $G_{N,\sigma}(V_{sd})$ obtained numerically for some representative sets of the model parameters.

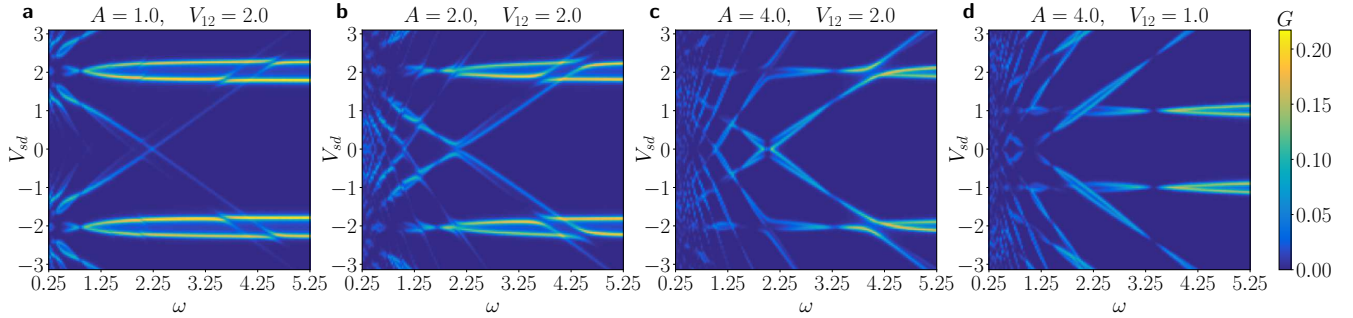


Figure 9. Frequency dependent conductance. The averaged Andreev conductance $G_{N,\sigma}(V_{sd})$ in units of $2e^2/h$ as a function of frequency ω and the source-drain voltage V_{sd} obtained for several amplitudes A and interdot coupling V_{12} (as indicated). We used the model parameters $\Gamma_N = 0.1$ and $\Gamma_S = 1.0$.

Fig. 9 presents the averaged Andreev conductance obtained for two values of the interdot coupling V_{12} and several amplitudes A , as indicated. Panels a-d display the characteristic features originating from the photon-assisted tunneling. We notice that besides the main quasiparticle peaks (for $\Gamma_N \ll \Gamma_S$ and $\epsilon_d = 0$ appearing at $\pm \frac{1}{2} \left(\sqrt{4V_{12}^2 + \Gamma_S^2/4} \pm \Gamma_S/2 \right)$ there emerge additional side-peaks due to the stimulated emission/absorption of the photon quanta. Their intensity (spectral weight) and avoided-crossing behavior are sensitive to the frequency and amplitude of a microwave field. The main quasiparticle peaks are replicated at multiples of ω and they can be interpreted as higher order harmonics of the initial bound states.

Basic aspects of the photon-assisted tunneling through the quantum dots sandwiched between the normal electrodes have been already extensively studied in specialistic literature⁵¹⁻⁵³. As regards the single quantum dot embedded into the superconducting heterostructures, it has been shown that n -th harmonic quasiparticle peaks would be proportional to the Bessel functions of the first kind $J_n^2(A/\omega)$ for the Andreev (N-QD-S) or $J_n^2(2A/\omega)$ for the Josephson (S-QD-S) circuits^{45,46}. Here the higher harmonics of the main quasiparticle peaks emerge at such amplitude A and frequency ω where the Bessel function $J_0(2A/\omega)$ vanishes. They do not depend on interdot coupling V_{12} . Frequencies corresponding to the lowest order harmonics for $A = 1$ occur at $\omega \sim 0.83, 0.36$, for $A = 2$ at $\omega \sim 1.67, 0.72, 0.46$ and for $A = 4$ at $\omega \sim 3.3, 1.45, 0.92$, respectively. Figs. 9 and 10 illustrate dependence of such side-peaks on the frequency ω and amplitude A , respectively.

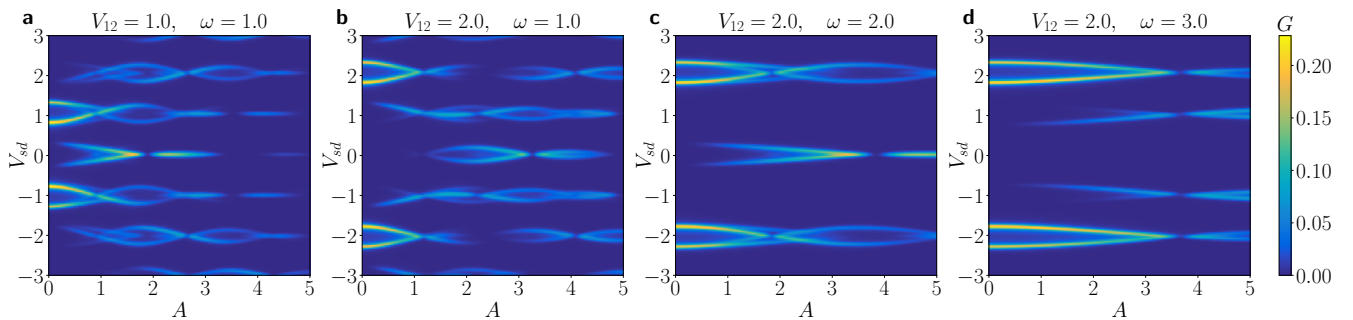


Figure 10. Amplitude dependent conductance. The averaged conductance $G_{N,\sigma}(V_{sd})$ versus the source-drain voltage V_{sd} and the amplitude A of the oscillating quantum dot levels obtained for several V_{12} and ω (as indicated), using the model parameters $\omega = 1.0$, $\Gamma_N = 0.1$, $\Gamma_S = 1.0$.

Let us consider the averaged Andreev conductance with respect to (V_{sd}, A) for a few values of the interdot coupling V_{12} , see Fig. 10. In absence of the microwave field, $A = 0$, there exist four peaks in the differential conductance. Upon increasing the power of microwave field (for larger amplitude A) the main quasiparticle peaks loose part their intensities (spectral weights) at expense of the higher order replicas. For larger amplitude A , we observe more and more replicas at $\omega, \pm\omega, \pm 2\omega$, and so on appearing in the conductance and simultaneously their total spectral weight undergoes substantial redistribution. At some

specific values of A we can notice that the spectral weight of individual harmonics vanishes and then again reappears.

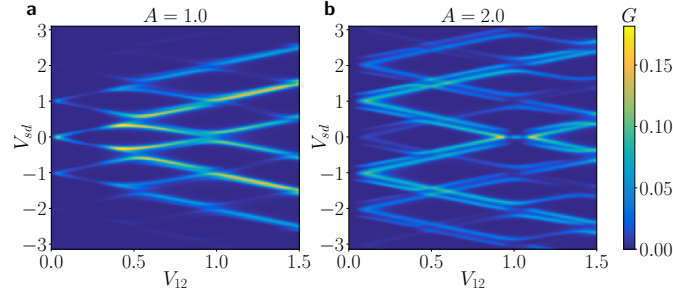


Figure 11. Dependence on interdot coupling. Variation of the averaged Andreev conductance $G_{N,\sigma}(V_{sd})$ with respect to the interdot coupling V_{12} obtained for $\omega = 1$, $\Gamma_N = 0.1$, $\Gamma_S = 1.0$, assuming $A = 1$ (left panel) and $A = 2$ (right panel).

To study the effect of inter-dot coupling on the averaged Andreev conductance we present in Fig. 11 the results obtained for $\omega = 1$ and two amplitudes $A = 1$ and $A = 2$, respectively. In the first case the conduction peaks, appearing around $\pm n\omega$, gradually split into the lower and upper branches with increasing coupling V_{12} , yet they never cross each other because of the quantum mechanical interference⁵⁴. For the larger amplitude ($A = 2$) we also notice this avoided-crossing tendency, albeit each harmonic consists here of two nearby peaks. This is example of the n -fold fine structure driven in the harmonics whenever the specific constraint $A/\omega = n$ is encountered.

In addition to direct computations of the averaged current, we have developed the auxiliary procedure based on machine learning algorithm which reliably yields the Andreev conductance for an arbitrary set of the model parameters (see *Methods*).

Discussion

We have studied the double quantum dot coupled between the superconducting and normal leads, addressing the dynamical response of such heterostructure to (i) abrupt application of the bias voltage, (ii) sudden change of the energy levels, and (iii) their periodic driving. These effects can be routinely triggered either by *dc* or *ac* external potentials. We have analyzed the time-dependent charge flow between the external reservoirs and the quantum dots, revealing the oscillatory behavior (analogous to Rabi-type mechanism involving pairs of the in-gap quasiparticle states induced by the superconducting proximity effect) which are damped due to relaxation on electronic states of the metallic lead.

Inspecting the time-dependent profiles of various physical observables we have found the signatures of such frequency components which coincide with the subgap quasiparticle energies. For the quantum quench imposed by the source-drain voltage and by the gate potential the dynamics of proximitized double quantum dot reveals superposition of the fast and slow oscillatory modes, giving rise to the beating patterns. These features are well observable over quite long time interval, $\Delta t \sim 10\hbar/\Gamma_N$, in contrast to much faster transient phenomena realized in the single quantum dot (N-QD-S) heterostructures^{48,55}.

For the periodically driven energy levels of the quantum dots we find more complex time-dependent behavior. Response of the N-DQD-S heterostructure depends both on the frequency ω and amplitude A of the periodically varying levels. We have illustrated these phenomena in absence (Figs. 6-8) and in presence of the bias voltage (Figs. 9-11). We have predicted that amplitude (related to the power of driving force) has crucial effect on activating the higher-order harmonics of in-gap quasiparticle states, as evidenced for the unbiased (Fig. 6) and biased (Fig. 10) heterostructures. The frequency, on the other hand, is manifested by replicas of the main quasiparticle peaks. Similar effects have been already observed experimentally for the Josephson-type junctions comprising the single quantum dot^{45,46}. In our case the proximitized double quantum dot is characterized a sequence of the photon-assisted enhancements in the differential conductance with an additional fine-structure appearing in the harmonics due to interference effects. Upon varying the frequency (Figs. 9) or the interdot coupling (Figs. 11) the neighboring harmonics never cross each other because of their quantum mechanical interplay, feasible also in the multi-terminal superconducting junctions⁵⁴.

Our considerations could be verified experimentally by means of the subgap tunneling spectroscopy using the carbon nanotubes, semiconducting nanowires or other lithographically constructed quantum dots embedded between the superconducting and metallic electrodes. Another realization would be possible in STM technique, using the conducting tip to probe the dimerized molecules deposited on superconducting substrates. The characteristic time-scales determined here might be important for designing logical operations with use of the superconducting qubits⁸. In future studies it would be worthwhile to address the dynamics of the topologically nontrivial superconducting nanostructures and take into account the Coulomb interaction effects.

1 ACKNOWLEDGEMENTS

This work was supported by the National Science Centre (NCN, Poland) under grants UMO-2017/27/B/ST3/01911 (B.B., R.T.) and UMO-2018/29/B/ST3/00937 (T.D.).

Methods

Equations of motion

Here, we explicitly present the set of differential equations needed for determination of the time-dependent occupancy $n_{i\sigma}(t) = \langle c_{i\sigma}^\dagger(t)c_{i\sigma}(t) \rangle$ and other functions coupled to it. Using the exact formula

$$c_{N\mathbf{k}\sigma}(t) = c_{N\mathbf{k}\sigma}(0) \exp\left(-i \int_0^t dt' \varepsilon_{N\mathbf{k}\sigma}(t')\right) - i \int_0^t dt' c_{2\sigma}(t') V_{N\mathbf{k}} \exp\left(-i \int_{t'}^t d\tau \varepsilon_{N\mathbf{k}\sigma}(\tau)\right) \quad (7)$$

and applying the wide band limit approximation we derive the following set of equations

$$\frac{dn_{1\sigma}(t)}{dt} = 2\text{Im}(V_{12} \langle c_{1\sigma}^\dagger(t)c_{2\sigma}(t) \rangle - \frac{\Gamma_S}{2} \langle c_{1-\sigma}(t)c_{1\sigma}(t) \rangle), \quad (8)$$

$$\frac{dn_{2\sigma}(t)}{dt} = 2\text{Im}[-V_{12} \langle c_{1\sigma}^\dagger(t)c_{2\sigma}(t) \rangle - \frac{i\Gamma_N}{2} n_{2\sigma}(t) + \sum_{\mathbf{k}} V_{N\mathbf{k}} \exp(-i\varepsilon_{N\mathbf{k}t}) \langle c_{2\sigma}^\dagger(t)c_{N\mathbf{k}\sigma}(0) \rangle \beta], \quad (9)$$

$$\begin{aligned} \frac{d\langle c_{1\sigma}(t)c_{2-\sigma}(t) \rangle}{dt} &= \left[-i(\varepsilon_{1\sigma} + \varepsilon_{2-\sigma}) - \frac{\Gamma_N}{2}\right] \langle c_{1\sigma}(t)c_{2-\sigma}(t) \rangle - iV_{12} (\langle c_{1\sigma}(t)c_{1-\sigma}(t) \rangle + \langle c_{2\sigma}(t)c_{2-\sigma}(t) \rangle) \\ &\quad + \alpha i \frac{\Gamma_S}{2} \langle c_{1-\sigma}^\dagger(t)c_{2-\sigma}(t) \rangle - i \sum_{\mathbf{k}} V_{N\mathbf{k}} \exp(-i\varepsilon_{N\mathbf{k}t}) \langle c_{1\sigma}(t)c_{N\mathbf{k}-\sigma}(0) \rangle \beta, \end{aligned} \quad (10)$$

$$\begin{aligned} \frac{d\langle c_{1\downarrow}(t)c_{1\uparrow}(t) \rangle}{dt} &= -i(\varepsilon_{1\uparrow} + \varepsilon_{1\downarrow}) \langle c_{1\downarrow}(t)c_{1\uparrow}(t) \rangle - iV_{12} (\langle c_{1\downarrow}(t)c_{2\uparrow}(t) \rangle - \langle c_{1\uparrow}(t)c_{2\downarrow}(t) \rangle) \\ &\quad - i \frac{\Gamma_S}{2} (1 - n_{1\downarrow}(t) - n_{1\uparrow}(t)), \end{aligned} \quad (11)$$

$$\begin{aligned} \frac{d\langle c_{2\downarrow}(t)c_{2\uparrow}(t) \rangle}{dt} &= [-i(\varepsilon_{2\uparrow} + \varepsilon_{2\downarrow}) - \Gamma_N] \langle c_{2\downarrow}(t)c_{2\uparrow}(t) \rangle + iV_{12} (\langle c_{1\uparrow}(t)c_{2\downarrow}(t) \rangle - \langle c_{1\downarrow}(t)c_{2\uparrow}(t) \rangle) \\ &\quad + i \sum_{\mathbf{k}} V_{N\mathbf{k}} \exp(-i\varepsilon_{N\mathbf{k}t}) (\langle c_{2\uparrow}(t)c_{N\mathbf{k}\downarrow}(0) \rangle - \langle c_{2\downarrow}(t)c_{N\mathbf{k}\uparrow}(0) \rangle) \beta, \end{aligned} \quad (12)$$

$$\begin{aligned} \frac{d\langle c_{1\sigma}^\dagger(t)c_{2\sigma}(t) \rangle}{dt} &= \left[-i(\varepsilon_{2\sigma} - \varepsilon_{1\sigma}) - \frac{\Gamma_N}{2}\right] \langle c_{1\sigma}^\dagger(t)c_{2\sigma}(t) \rangle - iV_{12} (n_{1\sigma}(t) - n_{2\sigma}(t)) + \alpha i \frac{\Gamma_S}{2} \langle c_{1-\sigma}(t)c_{2\sigma}(t) \rangle \\ &\quad - i \sum_{\mathbf{k}} V_{N\mathbf{k}} \exp(-i\varepsilon_{N\mathbf{k}t}) \langle c_{1\sigma}^\dagger(t)c_{N\mathbf{k}\sigma}(0) \rangle \beta, \end{aligned} \quad (13)$$

where $\sigma = \uparrow (\downarrow)$, $\alpha = +(-)$, $\beta = \exp(-i(t - t_1)V_{sd})$, t_1 denotes the time at which the bias voltage V_{sd} is applied and $\langle \dots \rangle$ stands for the quantum statistical averaging. At this level there appear the new correlation functions $\langle A_{i\sigma}(t)B_{\mathbf{k}\sigma}(0) \rangle$, where A (B) corresponds to the creation or annihilation operator of electron in the quantum dots (the normal lead). These functions can be determined from the the following equations of motion

$$\frac{d\langle c_{1\sigma}^\dagger(t)c_{N\mathbf{k}\sigma}(0) \rangle}{dt} = i\varepsilon_{1\sigma} \langle c_{1\sigma}^\dagger(t)c_{N\mathbf{k}\sigma}(0) \rangle + iV_{12} \langle c_{2\sigma}^\dagger(t)c_{N\mathbf{k}\sigma}(0) \rangle + \alpha i \frac{\Gamma_S}{2} \langle c_{1-\sigma}(t)c_{N\mathbf{k}\sigma}(0) \rangle, \quad (14)$$

$$\frac{d\langle c_{1\sigma}(t)c_{N\mathbf{k}-\sigma}(0) \rangle}{dt} = -i\varepsilon_{1\sigma} \langle c_{1\sigma}(t)c_{N\mathbf{k}-\sigma}(0) \rangle - iV_{12} \langle c_{2\sigma}(t)c_{N\mathbf{k}-\sigma}(0) \rangle - \alpha i \frac{\Gamma_S}{2} \langle c_{1-\sigma}^\dagger(t)c_{N\mathbf{k}-\sigma}(0) \rangle, \quad (15)$$

$$\frac{d\langle c_{2\sigma}^\dagger(t)c_{N\mathbf{k}\sigma}(0) \rangle}{dt} = \left(i\varepsilon_{2\sigma} - \frac{\Gamma_N}{2}\right) \langle c_{2\sigma}^\dagger(t)c_{N\mathbf{k}\sigma}(0) \rangle + iV_{12} \langle c_{1\sigma}^\dagger(t)c_{N\mathbf{k}\sigma}(0) \rangle + iV_{N\mathbf{k}} e^{i\varepsilon_{N\mathbf{k}t}} \langle n_{\mathbf{k}\sigma}(0) \rangle \beta^{-1}, \quad (16)$$

$$\frac{d\langle c_{2\sigma}(t)c_{N\mathbf{k}-\sigma}(0) \rangle}{dt} = \left(-i\varepsilon_{2\sigma} - \frac{\Gamma_N}{2}\right) \langle c_{2\sigma}(t)c_{N\mathbf{k}-\sigma}(0) \rangle - iV_{12} \langle c_{1\sigma}(t)c_{N\mathbf{k}-\sigma}(0) \rangle, \quad (17)$$

where $\langle n_{\mathbf{k}\sigma}(0) \rangle = [1 + \exp((\varepsilon_{N\mathbf{k}\sigma} - \mu_N)/k_B T)]^{-1}$ is the Fermi distribution function for the normal lead electrons.

We have solved numerically these coupled differential equations (8-17) subject to the specific initial conditions. For convenience, we have assumed that till $t < 0$ both external reservoirs were isolated from the quantum dots. In next steps, we have calculated iteratively the time-dependent observables using the Runge Kutta algorithm with sufficiently dense equidistant temporal points $t \rightarrow t + \delta t \rightarrow \dots \rightarrow t + N\delta t \equiv t_f$.

Machine learning approach

Results presented in the main part of this paper have been obtained by solving the differential equations derived for N-DQD-S heterostructure. The computational procedure has been rather straightforward (see the preceding section), but required quite a lot of time and resources.

For instance to produce the conduction maps (Figs. 9-11) with 150×150 points resolution it takes approximately one week performing multiprocessing calculations on CPU 2x Xeon E5-2660 2.2GHz 16 cores/ 32 threads. This problem motivated us to construct a machine learning model for our system.

To train our neural network we have used the collected set of data of 76 different conductance maps (with different resolutions), giving us 971760 conductance data points. Subsequently, we have linearly interpolated every single map to doubly increase a number of the data points, finally giving us 3887040 data points. For this purpose we have used the open-source software for machine learning - Tensorflow with application programming interface - Keras.

This neural network has a character of the densely connected type, with 4 input parameters ($V_{12}, \omega, V_{sd}, A$) describing N-DQD-S setup and 1 single neuron on the output, specifying the averaged Andreev conductance $G_{N,\sigma}$. The neural network is composed of 4 hidden layers consisting of 2048, 1024, 512, 256 neurons, respectively. Every hidden layer has a dropout of 1% neurons (which helps to avoid over-fitting our model) and, as an activation function, we have used sigmoid function. One can notice that this neural network is large, because of non-linearity in the system. To train our neural network we have chosen $batch = 1024$ and $epoch = 600$, giving us the fidelity coefficient $R^2 = 0.987$. Fig. 12a compares the calculated $G_{N,\sigma}$ with respect to the value predicted by our neural network. Fig. 12 shows the conductance maps obtained from direct calculation (panel a) and by the neural network (panel b). This neural network model of N-DQD-S heterostructure is available at the following www.dropbox.com/sh/0hzs9im3d3bf0jr/AADRr3kltw2mOdCCCh8tedoIWa?dl=0 webpage.

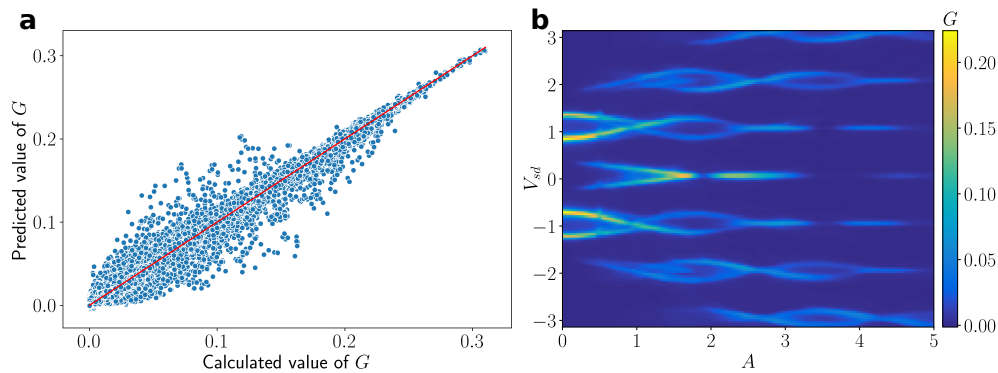


Figure 12. a) Comparison of the differential conductance predicted by the neural network versus its value determined by the microscopic calculations. The red line $y = x$ is a guide to eye. b) The conductance map generated by the neural network, reproducing the results presented in Fig.10a.

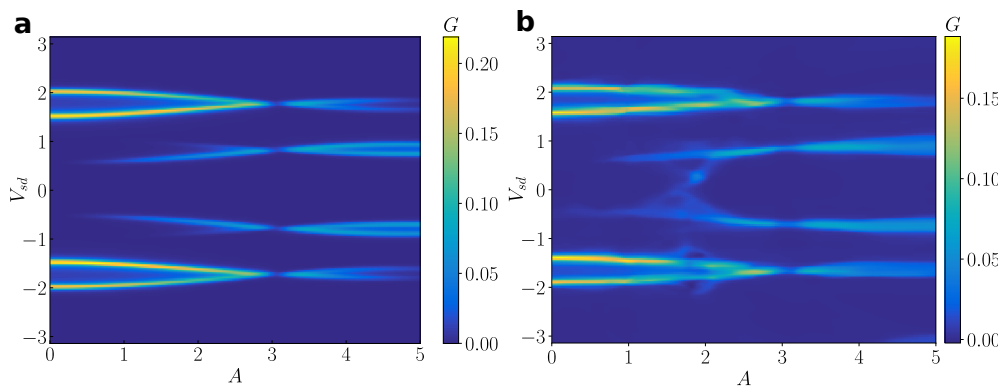


Figure 13. The conductance map obtained from the microscopic numerical calculations (panel a) and generated by the neural network (panel b) for $V_{12} = 1.7$, $\omega = 2.5$. The map shown in panel a has not been used for learning the neural network.

Author contributions statement

B.B. performed the numerical calculations, R.T. provided the methodological instruction, and T.D. coordinated this research project. All authors discussed the results and prepared the manuscript.

Additional information

Competing interests The authors declare no competing interests.

References

1. Nowack, K., Koppens, F., Nazarov, Y. & Vandersypen, L. Coherent control of a single electron spin with electric fields. *Science* **318**, 1430, DOI: [10.1126/science.1148092](https://doi.org/10.1126/science.1148092) (2007).
2. Nadj-Perge, S., Frolov, S., Bakkers, E. & Kouwenhoven, L. Spin-orbit qubit in a semiconductor nanowire. *Nature* **468**, 1084, DOI: [10.1038/nature09682](https://doi.org/10.1038/nature09682) (2010).
3. Antonov, I. V., Shaikhaidarov, R. S., Antonov, V. N. & Astafiev, O. V. Superconducting ‘twin’ qubit. *Phys. Rev. B* **102**, 115422, DOI: [10.1103/PhysRevB.102.115422](https://doi.org/10.1103/PhysRevB.102.115422) (2020).
4. Padurariu, C. & Nazarov, Y. V. Theoretical proposal for superconducting spin qubits. *Phys. Rev. B* **81**, 144519, DOI: [10.1103/PhysRevB.81.144519](https://doi.org/10.1103/PhysRevB.81.144519) (2010).
5. Larsen, T. W. *et al.* Parity-protected superconductor-semiconductor qubit. *Phys. Rev. Lett.* **125**, 056801, DOI: [10.1103/PhysRevLett.125.056801](https://doi.org/10.1103/PhysRevLett.125.056801) (2020).
6. Leijnse, M. & Flensberg, K. Parity qubits and poor man’s Majorana bound states in double quantum dots. *Phys. Rev. B* **86**, 134528, DOI: [10.1103/PhysRevB.86.134528](https://doi.org/10.1103/PhysRevB.86.134528) (2012).
7. Hyart, T. *et al.* Flux-controlled quantum computation with Majorana fermions. *Phys. Rev. B* **88**, 035121, DOI: [10.1103/PhysRevB.88.035121](https://doi.org/10.1103/PhysRevB.88.035121) (2013).
8. Aguado, R. A perspective on semiconductor-based superconducting qubits. *Appl. Phys. Lett.* **117**, 240501, DOI: [10.1063/5.0024124](https://doi.org/10.1063/5.0024124) (2020).
9. Chiorescu, I., Nakamura, Y., Harmans, C. J. P. M. & Mooij, J. E. Coherent quantum dynamics of a superconducting flux qubit. *Science* **299**, 1869–1871, DOI: [10.1126/science.1081045](https://doi.org/10.1126/science.1081045) (2003). <https://science.sciencemag.org/content/299/5614/1869.full.pdf>.
10. Balatsky, A. V., Vekhter, I. & Zhu, J.-X. Impurity-induced states in conventional and unconventional superconductors. *Rev. Mod. Phys.* **78**, 373, DOI: [10.1103/RevModPhys.78.373](https://doi.org/10.1103/RevModPhys.78.373) (2006).
11. Martín-Rodero, A. & Levy Yeyati, A. Josephson and Andreev transport through quantum dots. *Adv. Phys.* **60**, 899, DOI: [10.1080/00018732.2011.624266](https://doi.org/10.1080/00018732.2011.624266) (2011).
12. Prada, E. *et al.* From Andreev to Majorana bound states in hybrid superconductor-semiconductor nanowires. *Nat. Rev. Phys.* **2**, 575, DOI: [10.1038/s42254-020-0228-y](https://doi.org/10.1038/s42254-020-0228-y) (2020).
13. Sherman, D. *et al.* Normal, superconducting and topological regimes of hybrid double quantum dots. *Nat. Nanotechnol.* **12**, 212, DOI: [10.1038/nnano.2016.227](https://doi.org/10.1038/nnano.2016.227) (2017).
14. Grove-Rasmussen, K. *et al.* Yu-Shiba-Rusinov screening of spins in double quantum dots. *Nat. Commun.* **9**, 2376, DOI: [10.1038/s41467-018-04683-x](https://doi.org/10.1038/s41467-018-04683-x) (2018).
15. Estrada Saldaña, J. C. *et al.* Supercurrent in a double quantum dot. *Phys. Rev. Lett.* **121**, 257701, DOI: [10.1103/PhysRevLett.121.257701](https://doi.org/10.1103/PhysRevLett.121.257701) (2018).
16. Estrada Saldaña, J. C. *et al.* Two-impurity Yu-Shiba-Rusinov states in coupled quantum dots. *Phys. Rev. B* **102**, 195143, DOI: [10.1103/PhysRevB.102.195143](https://doi.org/10.1103/PhysRevB.102.195143) (2020).
17. Bouman, D. *et al.* Triplet-blockaded Josephson supercurrent in double quantum dots. *Phys. Rev. B* **102**, 220505, DOI: [10.1103/PhysRevB.102.220505](https://doi.org/10.1103/PhysRevB.102.220505) (2020).
18. Su, Z. *et al.* Andreev molecules in semiconductor nanowire double quantum dots. *Nat. Commun.* **8**, 585, DOI: [10.1038/s41467-017-00665-7](https://doi.org/10.1038/s41467-017-00665-7) (2017).
19. Zarassi, A. *et al.* Magnetic field evolution of spin blockade in Ge/Si nanowire double quantum dots. *Phys. Rev. B* **95**, 155416, DOI: [10.1103/PhysRevB.95.155416](https://doi.org/10.1103/PhysRevB.95.155416) (2017).
20. Cleuziou, J.-P., Wernsdorfer, W., Bouchiat, V., Ondarcuhu, T. & Monthieux, M. Carbon nanotube superconducting quantum interference device. *Nat. Nanotechnol.* **1**, 53, DOI: [10.1038/nnano.2006.54](https://doi.org/10.1038/nnano.2006.54) (2006).
21. Pillet, J.-D., Joyez, P., Žitko, R. & Goffman, M. F. Tunneling spectroscopy of a single quantum dot coupled to a superconductor: From Kondo ridge to Andreev bound states. *Phys. Rev. B* **88**, 045101, DOI: [10.1103/PhysRevB.88.045101](https://doi.org/10.1103/PhysRevB.88.045101) (2013).
22. Ruby, M., Heinrich, B., Peng, Y., von Oppen, F. & Franke, K. Wave-function hybridization in Yu-Shiba-Rusinov dimers. *Phys. Rev. Lett.* **120**, 156803, DOI: [10.1103/PhysRevLett.120.156803](https://doi.org/10.1103/PhysRevLett.120.156803) (2018).
23. Heinrich, B., Pascual, J. & Franke, K. Single magnetic adsorbates on s-wave superconductors. *Prog. Surf. Sci.* **93**, 1, DOI: <https://doi.org/10.1016/j.progsurf.2018.01.001> (2018).
24. Choi, D.-J. *et al.* Influence of magnetic ordering between Cr adatoms on the Yu-Shiba-Rusinov states of the β -Bi₂Pd superconductor. *Phys. Rev. Lett.* **120**, 167001, DOI: [10.1103/PhysRevLett.120.167001](https://doi.org/10.1103/PhysRevLett.120.167001) (2018).
25. Kezilebieke, S., Žitko, R., Dvorak, M. & Liljeroth, P. Observation of coexistence of Yu-Shiba-Rusinov states and spin-flip excitations. *Nano Lett.* **19**, 4614, DOI: [10.1021/acs.nanolett.9b01583](https://doi.org/10.1021/acs.nanolett.9b01583) (2019).

26. Choi, M.-S., Bruder, C. & Loss, D. Spin-dependent Josephson current through double quantum dots and measurement of entangled electron states. *Phys. Rev. B* **62**, 13569, DOI: [10.1103/PhysRevB.62.13569](https://doi.org/10.1103/PhysRevB.62.13569) (2000).
27. Zhu, Y., Sun, Q.-F. & Lin, T.-H. Probing spin states of coupled quantum dots by a dc Josephson current. *Phys. Rev. B* **66**, 085306, DOI: [10.1103/PhysRevB.66.085306](https://doi.org/10.1103/PhysRevB.66.085306) (2002).
28. Tanaka, Y., Kawakami, N. & Oguri, A. Correlated electron transport through double quantum dots coupled to normal and superconducting leads. *Phys. Rev. B* **81**, 075404, DOI: [10.1103/PhysRevB.81.075404](https://doi.org/10.1103/PhysRevB.81.075404) (2010).
29. Žitko, R., Lee, M., López, R., Aguado, R. & Choi, M.-S. Josephson current in strongly correlated double quantum dots. *Phys. Rev. Lett.* **105**, 116803, DOI: [10.1103/PhysRevLett.105.116803](https://doi.org/10.1103/PhysRevLett.105.116803) (2010).
30. Eldridge, J., Pala, M., Governale, M. & König, J. Superconducting proximity effect in interacting double-dot systems. *Phys. Rev. B* **82**, 184507, DOI: [10.1103/PhysRevB.82.184507](https://doi.org/10.1103/PhysRevB.82.184507) (2010).
31. Droste, S., Andergassen, S. & Splettstoesser, J. Josephson current through interacting double quantum dots with spin-orbit coupling. *J. Phys.: Condens. Matter* **24**, 415301, DOI: [10.1088/0953-8984/24/41/415301](https://doi.org/10.1088/0953-8984/24/41/415301) (2012).
32. Pfaller, S., Donarini, A. & Grifoni, M. Subgap features due to quasiparticle tunneling in quantum dots coupled to superconducting leads. *Phys. Rev. B* **87**, 155439, DOI: [10.1103/PhysRevB.87.155439](https://doi.org/10.1103/PhysRevB.87.155439) (2013).
33. Brunetti, A., Zazunov, A., Kundu, A. & Egger, R. Anomalous Josephson current, incipient time-reversal symmetry breaking, and Majorana bound states in interacting multilevel dots. *Phys. Rev. B* **88**, 144515, DOI: [10.1103/PhysRevB.88.144515](https://doi.org/10.1103/PhysRevB.88.144515) (2013).
34. Sothmann, B., Weiss, S., Governale, M. & König, J. Unconventional superconductivity in double quantum dots. *Phys. Rev. B* **90**, 220501, DOI: [10.1103/PhysRevB.90.220501](https://doi.org/10.1103/PhysRevB.90.220501) (2014).
35. Meng, T., Klinovaja, J., Hoffman, S., Simon, P. & Loss, D. Superconducting gap renormalization around two magnetic impurities: From Shiba to Andreev bound states. *Phys. Rev. B* **92**, 064503, DOI: [10.1103/PhysRevB.92.064503](https://doi.org/10.1103/PhysRevB.92.064503) (2015).
36. Žitko, R. Numerical subgap spectroscopy of double quantum dots coupled to superconductors. *Phys. Rev. B* **91**, 165116, DOI: [10.1103/PhysRevB.91.165116](https://doi.org/10.1103/PhysRevB.91.165116) (2015).
37. Ptok, A., Głodzik, S. & Domański, T. Yu-Shiba-Rusinov states of impurities in a triangular lattice of NbSe₂ with spin-orbit coupling. *Phys. Rev. B* **96**, 184425, DOI: [10.1103/PhysRevB.96.184425](https://doi.org/10.1103/PhysRevB.96.184425) (2017).
38. Pekker, D. & Frolov, S. Andreev blockade in a double quantum dot with a superconducting lead (2018). [1810.05112](https://arxiv.org/abs/1810.05112).
39. Scherübl, Z., Pályi, A. & Csonka, S. Transport signatures of an Andreev molecule in a quantum dot-superconductor-quantum dot setup. *Beilstein J. Nanotechnol.* **10**, 363, DOI: [10.3762/bjnano.10.36](https://doi.org/10.3762/bjnano.10.36) (2019).
40. Zalom, P., Pokorný, V. & Novotný, T. Spectral and transport properties of a half-filled anderson impurity coupled to phase-biased superconducting and metallic leads. *Phys. Rev. B* **103**, 035419, DOI: [10.1103/PhysRevB.103.035419](https://doi.org/10.1103/PhysRevB.103.035419) (2021).
41. Wang, X.-Q., Zhang, S.-F., Han, Y. & Gong, W.-J. Fano-Andreev effect in a parallel double quantum dot structure. *Phys. Rev. B* **100**, 115405, DOI: [10.1103/PhysRevB.100.115405](https://doi.org/10.1103/PhysRevB.100.115405) (2019).
42. Li, Z.-Z. & Leijnse, M. Quantum interference in transport through almost symmetric double quantum dots. *Phys. Rev. B* **99**, 125406, DOI: [10.1103/PhysRevB.99.125406](https://doi.org/10.1103/PhysRevB.99.125406) (2019).
43. Collura, M. & Essler, F. How order melts after quantum quenches. *Phys. Rev. B* **101**, 041110, DOI: [10.1103/PhysRevB.101.041110](https://doi.org/10.1103/PhysRevB.101.041110) (2020).
44. Taranko, R., Kwapiński, T. & Domański, T. Transient dynamics of a quantum dot embedded between two superconducting leads and a metallic reservoir. *Phys. Rev. B* **99**, 165419, DOI: [10.1103/PhysRevB.99.165419](https://doi.org/10.1103/PhysRevB.99.165419) (2019).
45. Kot, P. *et al.* Microwave-assisted tunneling and interference effects in superconducting junctions under fast driving signals. *Phys. Rev. B* **101**, 134507, DOI: [10.1103/PhysRevB.101.134507](https://doi.org/10.1103/PhysRevB.101.134507) (2020).
46. Peters, O. *et al.* Resonant Andreev reflections probed by photon-assisted tunnelling at the atomic scale. *Nat. Phys.* **16**, 1222–1226, DOI: [10.1038/s41567-020-0972-z](https://doi.org/10.1038/s41567-020-0972-z) (2020).
47. González, S. *et al.* Photon-assisted resonant Andreev reflections: Yu-Shiba-Rusinov and Majorana states. *Phys. Rev. B* **102**, 045413, DOI: [10.1103/PhysRevB.102.045413](https://doi.org/10.1103/PhysRevB.102.045413) (2020).
48. Taranko, R. & Domański, T. Buildup and transient oscillations of Andreev quasiparticles. *Phys. Rev. B* **98**, 075420, DOI: [10.1103/PhysRevB.98.075420](https://doi.org/10.1103/PhysRevB.98.075420) (2018).
49. Taranko, E., Wiertel, M. & Taranko, R. Transient electron transport properties of multiple quantum dots systems. *J. App. Phys.* **111**, 023711, DOI: [10.1063/1.3679050](https://doi.org/10.1063/1.3679050) (2012).
50. Baran, B. & Domański, T. Quasiparticles of a periodically driven quantum dot coupled between superconducting and normal leads. *Phys. Rev. B* **100**, 085414, DOI: [10.1103/PhysRevB.100.085414](https://doi.org/10.1103/PhysRevB.100.085414) (2019).
51. Jauho, A.-P., Wingreen, N. S. & Meir, Y. Time-dependent transport in interacting and noninteracting resonant-tunneling systems. *Phys. Rev. B* **50**, 5528–5544, DOI: [10.1103/PhysRevB.50.5528](https://doi.org/10.1103/PhysRevB.50.5528) (1994).

52. Kwapiński, T., Taranko, R. & Taranko, E. Photon-assisted electron transport through a three-terminal quantum dot system with nonresonant tunneling channels. *Phys. Rev. B* **72**, 125312, DOI: [10.1103/PhysRevB.72.125312](https://doi.org/10.1103/PhysRevB.72.125312) (2005).
53. Platero, G. & Aguado, R. Photon-assisted transport in semiconductor nanostructures. *Phys. Reports* **395**, 1 – 157, DOI: <https://doi.org/10.1016/j.physrep.2004.01.004> (2004).
54. Mélin, R. & Douçot, B. Inversion in a four-terminal superconducting device on the quartet line. ii. quantum dot and Floquet theory. *Phys. Rev. B* **102**, 245436, DOI: [10.1103/PhysRevB.102.245436](https://doi.org/10.1103/PhysRevB.102.245436) (2020).
55. Souto, R. S., Martín-Rodero, A. & Yeyati, A. L. Quench dynamics in superconducting nanojunctions: Metastability and dynamical Yang-Lee zeros. *Phys. Rev. B* **96**, 165444, DOI: [10.1103/PhysRevB.96.165444](https://doi.org/10.1103/PhysRevB.96.165444) (2017).

Figures

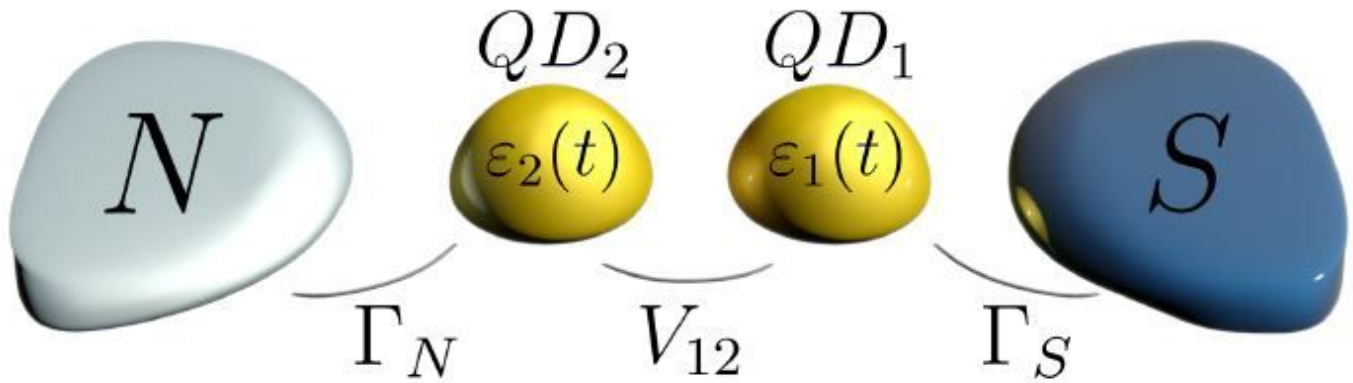


Figure 1

Schematics. Two quantum dots (QD1 and QD2) coupled in series between the superconducting (S) and normal (N) metallic reservoirs whose energy levels $\epsilon_{i\sigma}(t)$ could be varied by the external gate potential. We also consider dynamical phenomena driven by the time-dependent bias voltage imposed between the external leads.

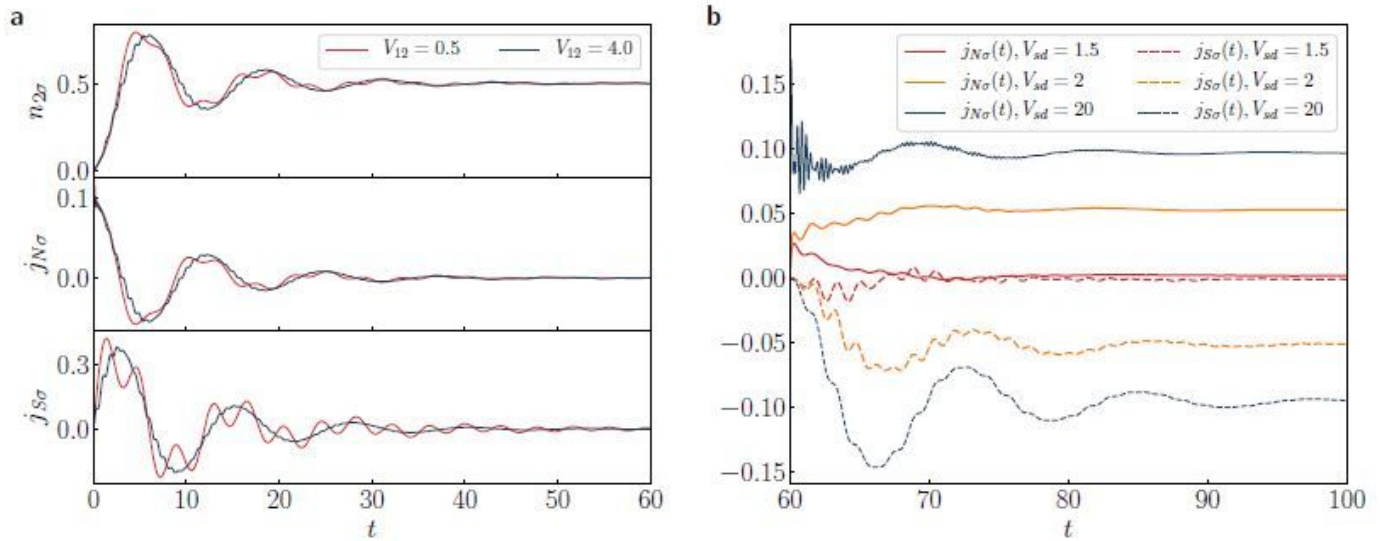


Figure 2

Transient and quench dynamics. a) The time-dependent $n_{2\sigma}$, $j_{S\sigma}$ and $j_{N\sigma}$ obtained for $V_{12} = 0.5, 4$, assuming the initially empty DQDs. b) The charge currents $j_{S\sigma}$ and $j_{N\sigma}$ for $V_{12} = 2$ induced after an abrupt biasing V_{sd} at $t = 60$. Calculations have been done for $G_N = 0.2$, $G_S = 1$, $\epsilon_{i\sigma} = 0$.

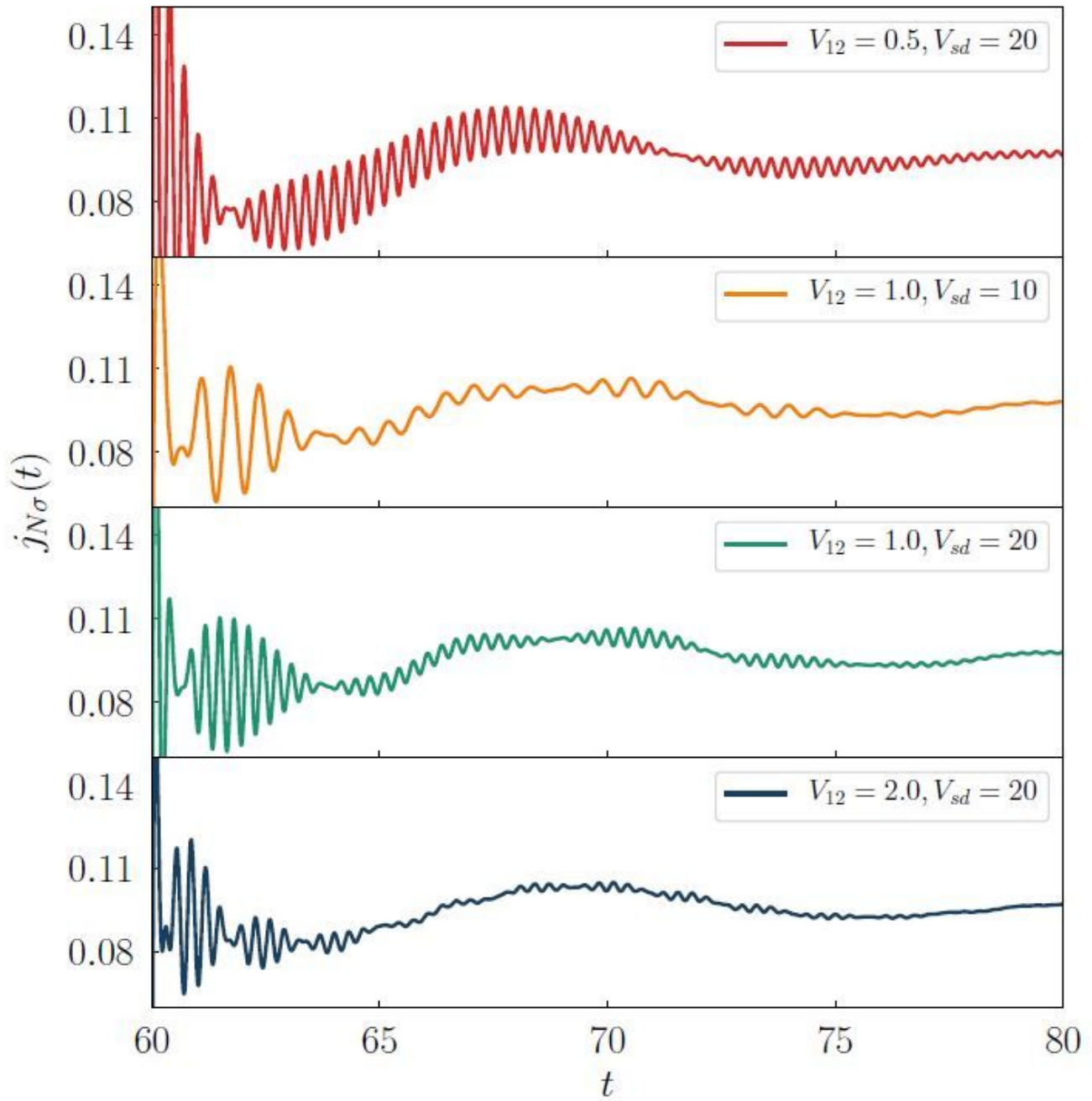


Figure 3

Post-quench beating patterns. The current $j_{N\sigma}(t)$ induced by abrupt biasing at $t = 60$ for several values of the interdot coupling V_{12} and V_{sd} , as indicated. We used the model parameters $GN = 0.2, GS = 1, eis = 0$.

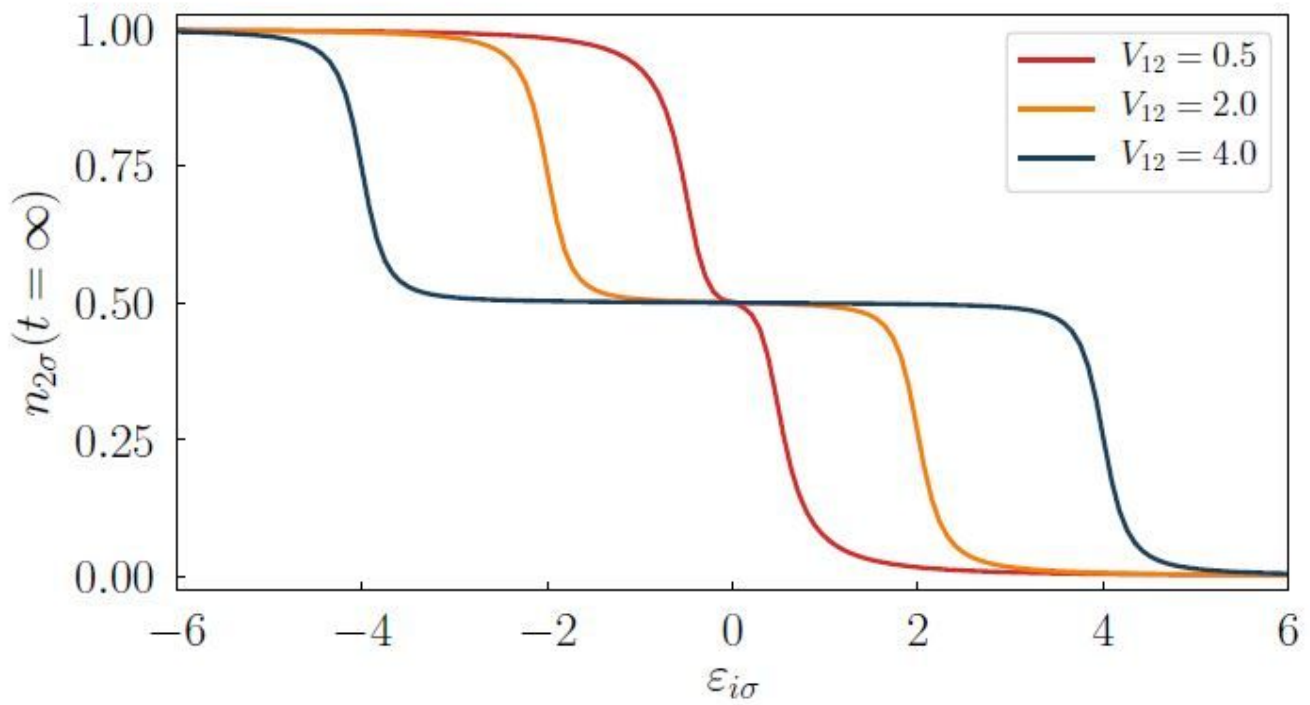


Figure 4

Charge occupancy. The stationary limit ($t = \infty$) occupancy of QD2 as a function of the energy level $e_{2s} = e_{1s}$ determined for several interdot couplings V_{12} using the model parameters $V_{sd} = 0$, $G_N = 0.1$, $G_S = 1$.

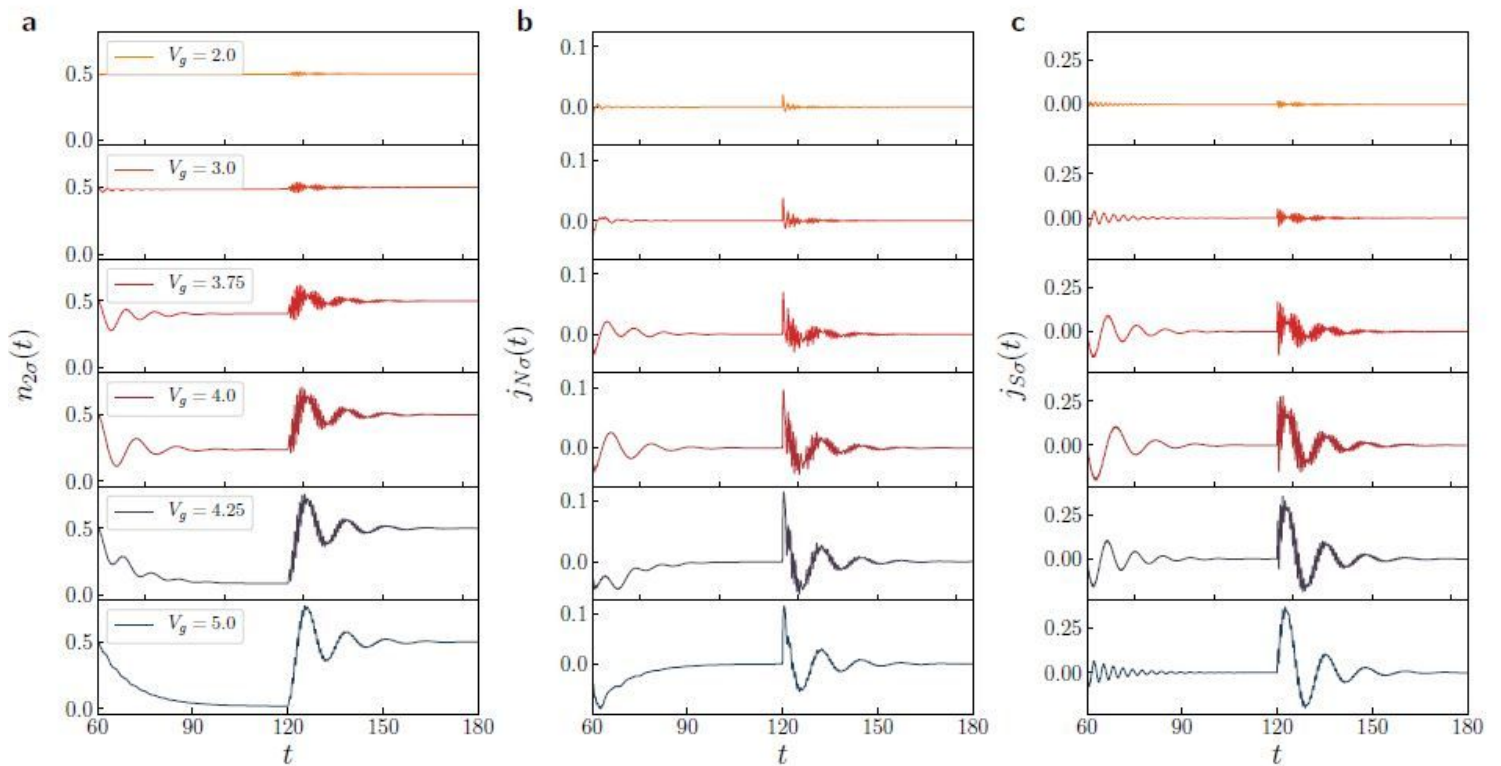


Figure 5

Dynamics imposed by varying the energy levels. The time-dependent occupancy $n_{2s}(t)$ and the currents $j_{Ns}(t)$, $j_{Ss}(t)$ after step-like variation of the quantum dots energy levels $\epsilon_{is} \rightarrow \epsilon_{is} + Vg$ at $t = 60$ and $Vg \rightarrow \epsilon_{is}$ at $t = 120$. Results are obtained for $V_{sd} = 0$, $GN = 0:2$, $GS = 1$, $\epsilon_{is} = 0$ and $V_{12} = 4$.

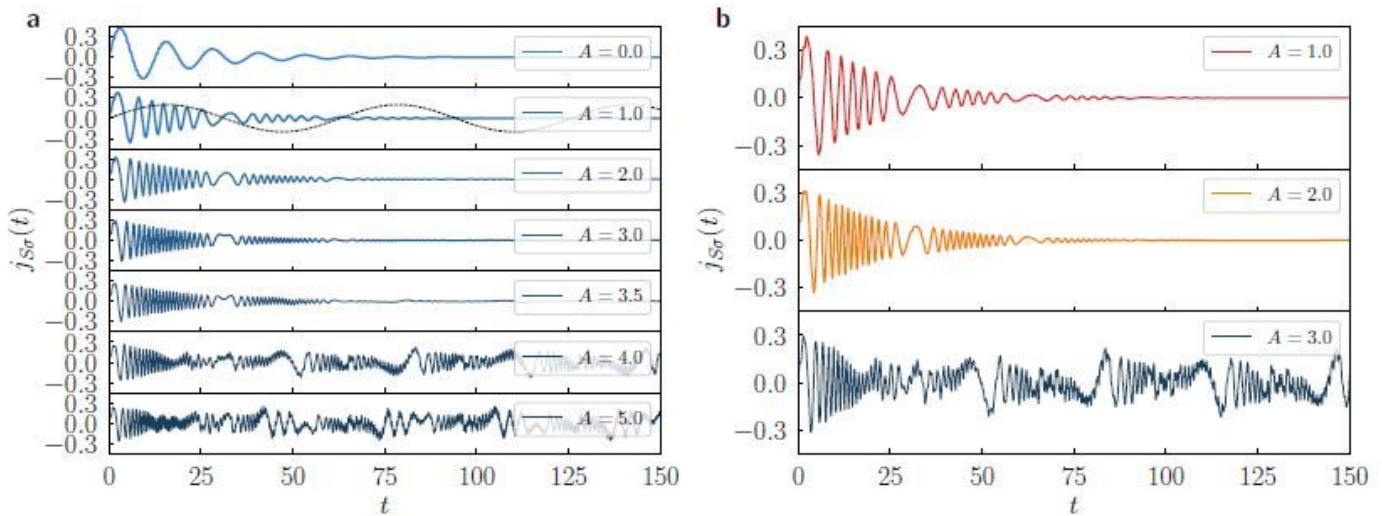


Figure 6

Amplitude effect of periodic driving. The time-dependent current j_{Ss} induced by the oscillating energy levels $\epsilon_{is}(t) = A \sin(\omega t)$. The panel a (b) presents the results obtained for $V_{12} = 4:0$ ($V_{12} = 3:0$), assuming $\omega = 0:1$, $GN = 0:1$, $GS = 1$, $V_{sd} = 0$ and several amplitudes A . The dashed line shows the profile of the oscillations energy levels (not in scale).

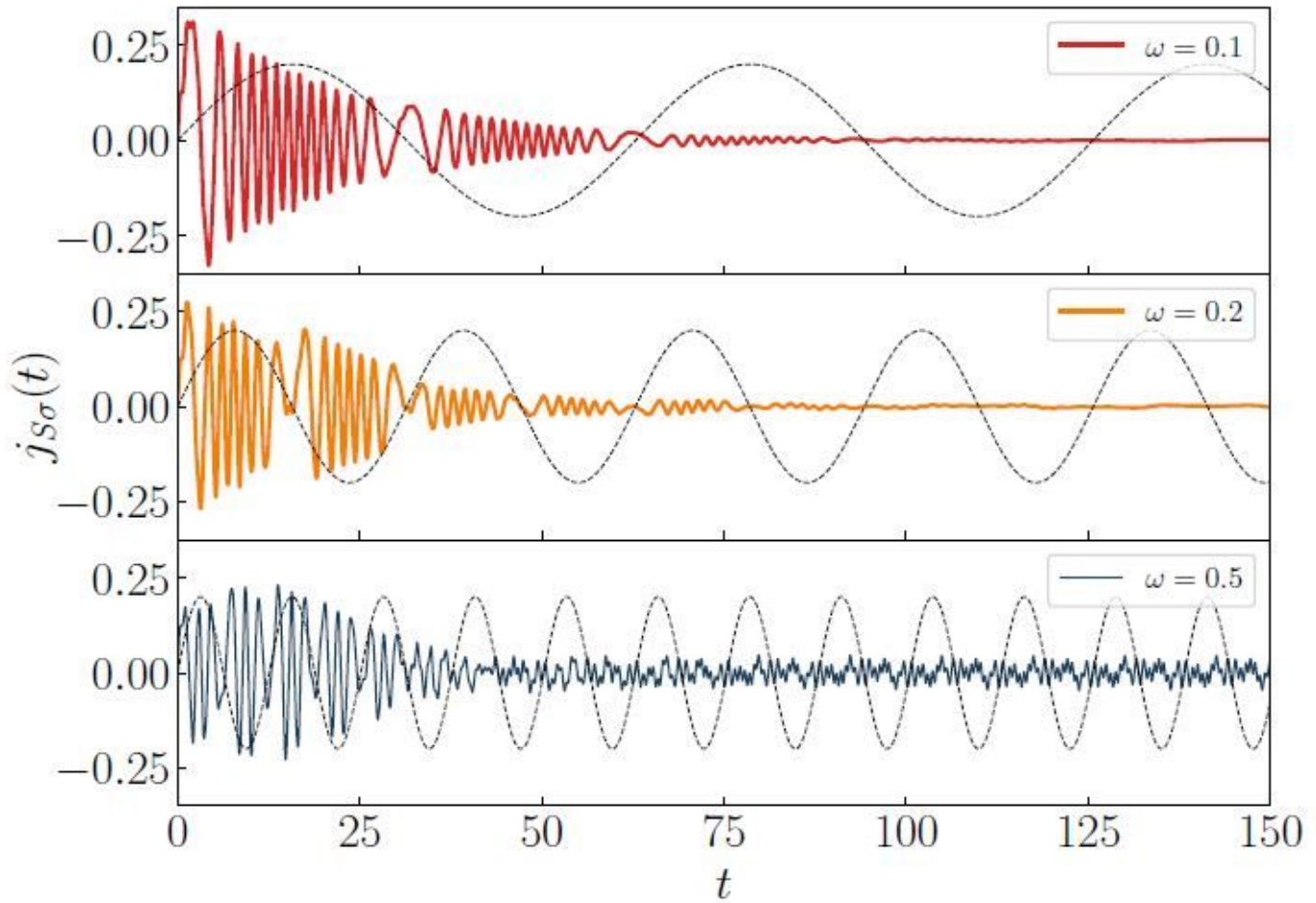


Figure 7

Frequency effect of periodic driving. The time-dependent current $j_{S\sigma}$ caused by periodic driving of the QD levels for several frequencies ω (as indicated), assuming $V_{12} = 3:0$, $A = 2:0$, $GN = 0:1$, $GS = 1:0$, $V_{sd} = 0$.

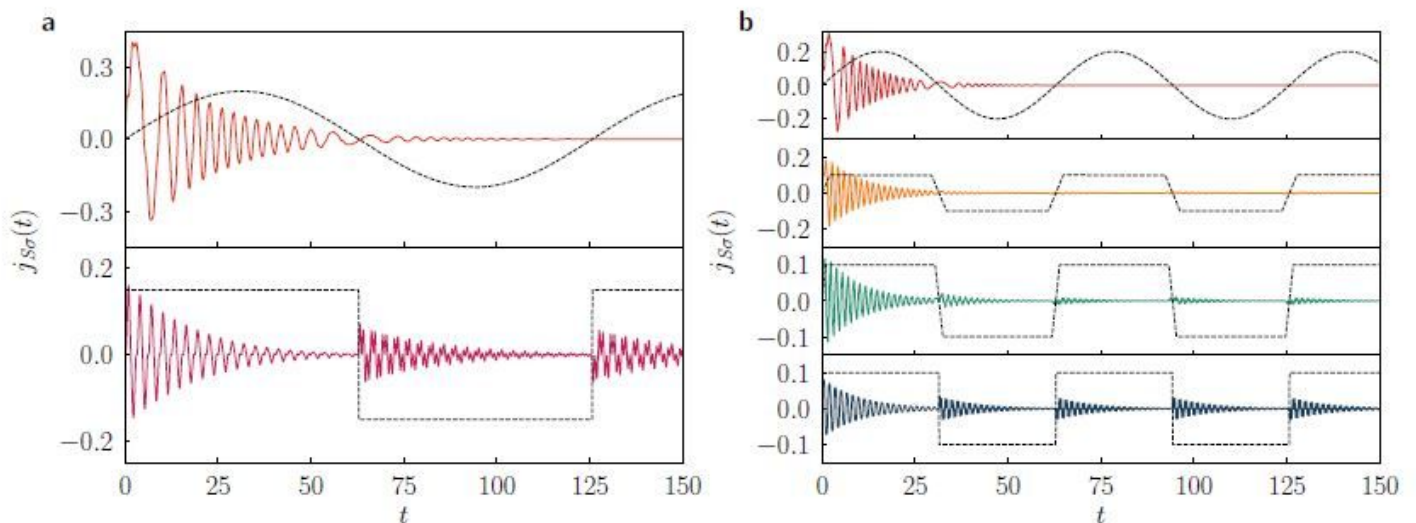


Figure 8

Various protocols of periodic driving. The time-dependent current j_s s (solid lines) obtained for different periodic driving schemes $\epsilon_i s(t)$ (dotted lines, not in scale). The panel a (b) shows the results for $V_{12} = 2:0$, $A = 1:0$ and $w = 0:05$ ($V_{12} = 4:0$, $A = 2:0$ and $w = 0:1$), using the model parameters $GN = 0:2$, $GS = 1:0$, $V_{sd} = 0$.

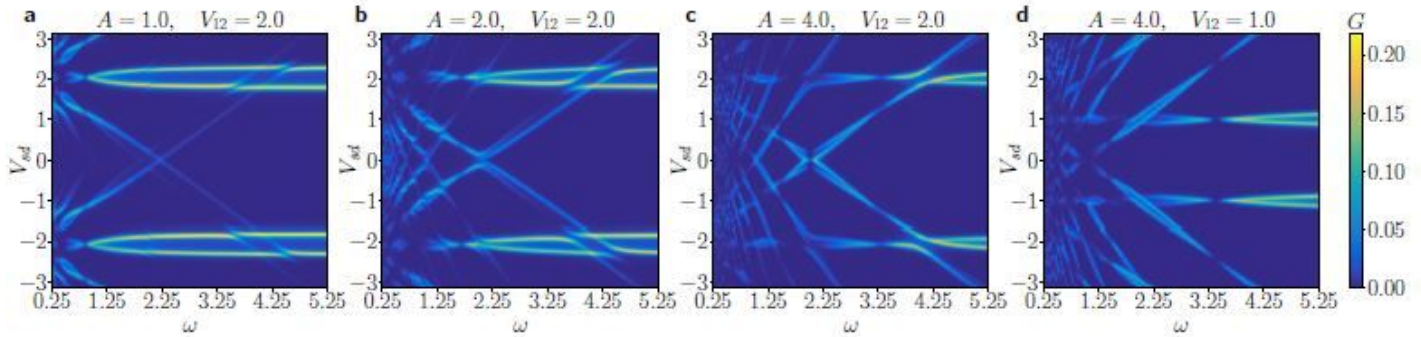


Figure 9

Frequency dependent conductance. The averaged Andreev conductance $GN_s(V_{sd})$ in units of $2e^2 = h$ as a function of frequency w and the source-drain voltage V_{sd} obtained for several amplitudes A and interdot coupling V_{12} (as indicated). We used the model parameters $GN = 0:1$ and $GS = 1:0$.

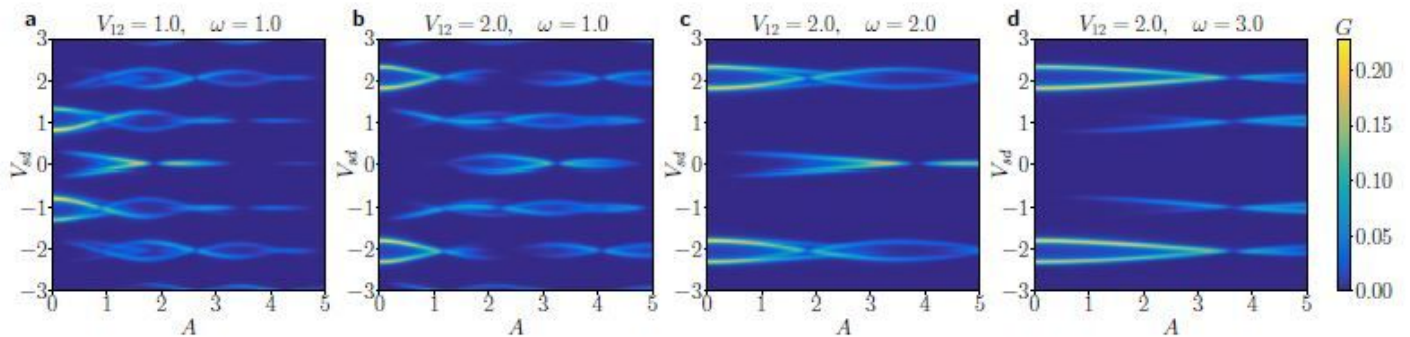


Figure 10

Amplitude dependent conductance. The averaged conductance $GN_s(V_{sd})$ versus the source-drain voltage V_{sd} and the amplitude A of the oscillating quantum dot levels obtained for several V_{12} and w (as indicated), using the model parameters $w = 1:0$, $GN = 0:1$, $GS = 1:0$.

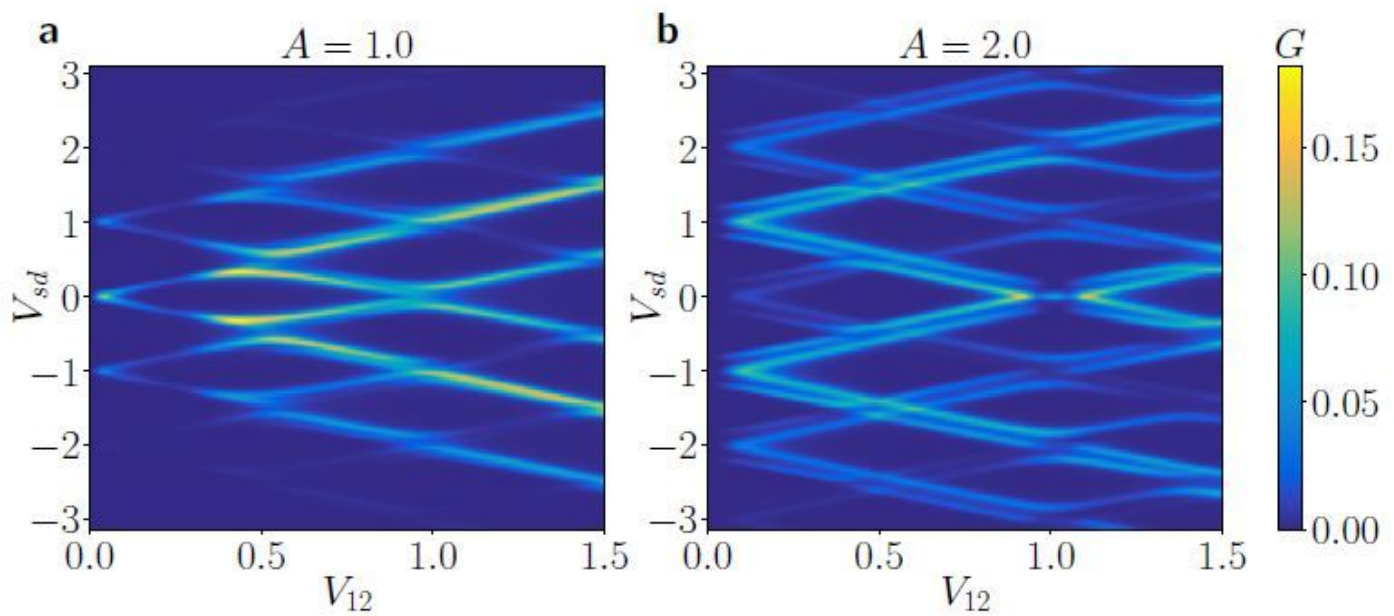


Figure 11

Dependence on interdot coupling. Variation of the averaged Andreev conductance G_N 's (V_{sd}) with respect to the interdot coupling V_{12} obtained for $w = 1$, $G_N = 0:1$, $G_S = 1:0$, assuming $A = 1$ (left panel) and $A = 2$ (right panel).

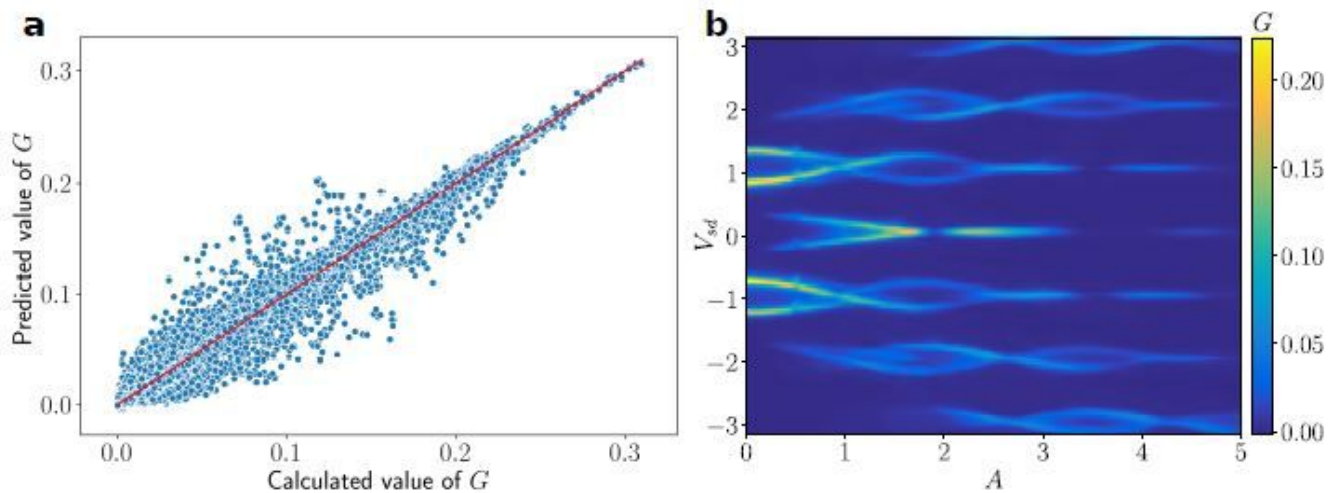


Figure 12

a) Comparison of the differential conductance predicted by the neural network versus its value determined by the microscopic calculations. The red line $y = x$ is a guide to eye. b) The conductance map generated by the neural network, reproducing the results presented in Fig.10a.

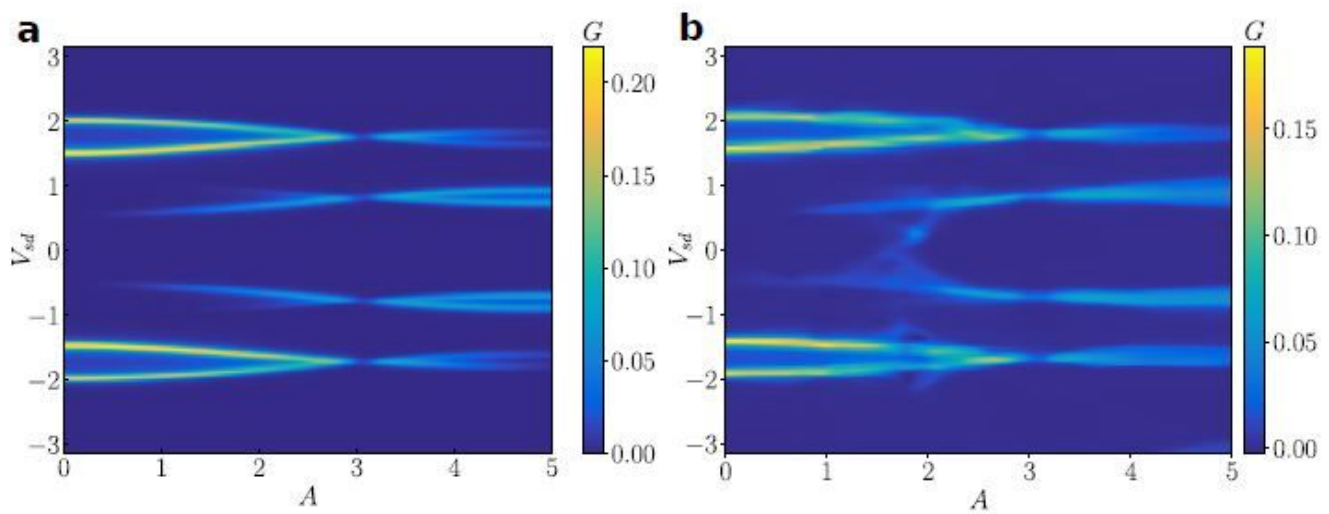


Figure 13

The conductance map obtained from the microscopic numerical calculations (panel a) and generated by the neural network (panel b) for $V_{12} = 1:7$, $w = 2:5$. The map shown in panel a has not been used for learning the neural network.